Single *in situ* intratumoral low-dose shikonin hydrogel plus mild photothermal therapy elicits systemic antitumor immunity in immune-cold triple-negative breast cancer

TAO PAN[1*], ZUJIAN FENG[2*], TING SHANG[1*], JUN JIANG[3] and FANG ZHANG[4]

[1]Department of Respiratory and Critical Care Medicine, Xijing Hospital, Air Force Medical University, Xi'an, Shaanxi 710032, P.R. China; [2]Tianjin Key Laboratory of Biomaterial Research, Institute of Biomedical Engineering, Chinese Academy of Medical Sciences and Peking Union Medical College, Tianjin 300192, P.R. China; [3]Department of Health Service, Air Force Medical University, Xi'an, Shaanxi 710032, P.R. China; [4]The Second Affiliated Hospital of Xi'an Medical University, Xi'an, Shaanxi 710038, P.R. China

Received March 24, 2026; Accepted August 3, 2026

DOI: 10.3892/ijo.2026.5930

Abstract. Shikonin (SHK) possesses potent antitumor activity; however, its severe non-selective toxicity greatly limits the feasibility of conventional systemic administration for cancer therapy. Likewise, mild photothermal therapy (PTT) has intrinsic limitations, including inadequate induction of immunogenic cell death (ICD) and compensatory activation of immunosuppressive pathways, such as increased IDO1 activity and PD-L1 expression. In the present study, low-dose SHK and gold nanorods were co-encapsulated within a supramolecular hydrogel (mPECT) and administered by intratumoral injection to achieve localized combination therapy with mild PTT. Mild PTT rapidly triggered antitumor immune activation within the immunosuppressive tumor microenvironment, whereas SHK sustained this response by suppressing PTT-induced IDO1 activation and PD-L1 upregulation and by markedly enhancing ICD. The mPECT hydrogel enabled prolonged local retention and controlled release of SHK, minimizing rapid systemic exposure while preserving therapeutic efficacy at the tumor site. This localized combination of SHK and mild PTT elicited a robust adaptive antitumor immune response that not only inhibited primary tumor growth but also suppressed the progression of untreated distant tumors and generated durable antitumor immune memory. These findings indicate that a single intratumoral administration of low-dose SHK-loaded hydrogel combined with mild PTT can induce potent systemic antitumor immunity, supporting the further development of localized SHK-based therapeutic strategies for the treatment of immune-cold tumors.

Correspondence to: Dr Tao Pan, Department of Respiratory and Critical Care Medicine, Xijing Hospital, Air Force Medical University, 169 Changle West Road, Xincheng, Xi'an, Shaanxi 710032, P.R. China
E-mail: 1718536699@qq.com

Professor Fang Zhang, The Second Affiliated Hospital of Xi'an Medical University, 167 Fangdong Street, Baqiao, Xi'an, Shaanxi 710038, P.R. China
E-mail: 176177507@qq.com

*Contributed equally

Abbreviations: SHK, shikonin; PTT, photothermal therapy; ICD, immunogenic cell death; IDO1, indoleamine 2,3-dioxygenase 1; PD-L1, programmed death-ligand 1; TNBC, triple-negative breast cancer; mPECT, methoxy poly(ethylene glycol)-b-poly(ε-caprolactone-co-1,4,8-trioxa[4.6]spiro-9-undecanone); AuNRs, gold nanorods; NIR, near-infrared irradiation; DAMPs, damage-associated molecular patterns; APCs, antigen-presenting cells; CRT, calreticulin; HMGB1, high mobility group box 1; Kyn, kynurenine; Trp, tryptophan; DC, dendritic cell; TILs, tumor-infiltrating lymphocytes; TDLNs, tumor-draining lymph nodes; Treg, regulatory T cell; qPCR, quantitative polymerase chain reaction; ELISA, enzyme-linked immunosorbent assay; CYT, cytolytic activity

Key words: SHK, intratumoral administration, hydrogel, mild PTT, immunogenic cell death, PD-L1, IDO1, abscopal effect, immune memory, TNBC

Introduction

SHK is the main active compound of traditional Chinese herb Zicao (the dried root of *Lithospermum erythrorhizon*), which has been shown to exert diverse antitumor effects. SHK can induce autophagy, apoptosis and necroptosis in multiple types of cancer cells (1). SHK can also suppress the invasion, migration and metastasis of cancer cells, inhibit angiogenesis, affect metabolic reprogramming, and promote cell cycle arrest (2,3). Indeed, a large number of studies have investigated the antitumor effects of SHK over the past three decades, and nearly 1,000 related publications have been published. However, due to its strong and non-selective toxicity, SHK has not yet been approved for the clinical treatment of tumors (4). Thus, there is an urgent need for therapeutic strategies that preserve the potent antitumor activity of SHK while minimizing its toxicity to normal tissues. Nanocarriers have emerged as promising platforms for cancer therapy (5). Encapsulating SHK within nanocarriers for systemic administration to enhance its

localized accumulation in tumor appears to be a promising direction (6). However, increasing evidence shows that when nanocarriers are administered through systemic circulation, a large proportion of nanocarriers still undergo phagocytosis through the mononuclear phagocyte system or even phagocytes around the tumor, leading to low drug concentrations at the tumor site (7). In the present study, for the first time, SHK was loaded into the sustained-release hydrogel for intratumoral injection, to ensure direct and sustained exposure of local tumors to SHK. This strategy can prevent the high-concentration SHK from entering into the systemic circulation and reduce the toxic damage to normal tissues.

Several studies have found that SHK can strongly induce immunogenic cell death (ICD) in cancer cells. Unlike apoptosis, ICD not only releases a large number of tumor-specific antigens, but also damage-associated molecular patterns (DAMPs), which activates antigen presenting cells (APCs) and triggers the process of tumor antigen presentation, eventually promoting the expansion of tumor-specific T cells (8). Furthermore, it has been reported that SHK reduces the content of lactic acid in the tumor microenvironment (TME) by inhibiting pyruvate kinase (9), promotes the transformation of M2 subtype macrophages to the M1 subtype (10), and inhibits IDO1 catalytic activity through interaction with the ferric form of IDO1 (11). All these data suggest that SHK has favorable potential in reversing the tumor immunosuppressive microenvironment. Unfortunately, because of SHK's pharmacological properties in inhibiting the expression of a variety of immune promoting cytokines and the negative effects on immune activation (1,12), SHK alone is insufficient to activate an effective antitumor immune response in immune-cold tumors.

Photothermal therapy (PTT) has emerged as a novel paradigm for precise cancer medicine due to its advantages of controllable irradiation and temperature, non-invasiveness and localized treatment. Generally, photothermal heating to a high temperature of >50˚C is needed for achieving a harsh environment for tumor ablation (13). This excessive hyperthermia increases the risk of injuring the surrounding normal tissues and may trigger unwanted inflammation due to the problem of heat transfer. Since PTT compels tumor cells to death through necrosis at a temperature of >50˚C by releasing intracellular biomolecules and cellular fragments, aggressive local inflammation may occur, thus damaging healthy tissues and promoting tumor metastasis (14). Moreover, it should be noted that overheating at such high temperature may reduce the production of DAMPs in the TME, leading to insufficient recruitment and activation of endogenous APCs, as well as disrupting the immune antigens that evoke antitumor immunity and immune cells that execute immune response in the TME (15). This, in turn, prevents the immune system from destroying cancer cells. To surmount these bottleneck problems, mild PTT (also referred to as mild-temperature or low-temperature PTT), which exerts multiple effects on local tumors at relatively low temperatures while minimizing damage to healthy tissues, has been proposed. In the present study, mild PTT was operationally defined as temperature-controlled local photothermal heating maintained at ~43˚C for 15 min. Theoretically, mild PTT is regarded as one of the important variables in constructing a favorable TME for triggering immune responses (16). Mild PTT can improve the infiltration of immune cells into tumors, increase the expression of immune-promoting cytokines in tumor site, and trigger a limited antitumor immunity (17). However, a slight increase in temperature alone may not be sufficient to induce widespread tumor cell death, which results in an inadequate supply of neoantigens for activating specific antitumor immunity. Moreover, this increase in temperature may potentially trigger the upregulation of PD-L1, IDO1, and heat shock proteins on tumor cells as part of their self-defense mechanisms. Such a feedback loop could potentially lead to an immunosuppressive effect, further hindering the desired antitumor immune response (18). Hence, the antitumor immunity evoked by mild PTT is generally limited and has a short lifespan (19). Therefore, it is important to explore the combination strategies for enhancing and prolonging the antitumor immunity triggered by mild PTT.

Triple-negative breast cancer (TNBC) is the most malignant subtype of breast cancer (BC), prone to spread faster and relapse after treatment (20). As these cancer cells do not express HER-2, progesterone receptor or estrogen receptor, there are only a few TNBC-targeted therapies available (20). A number of studies have shown that TNBC exhibits improved immunogenicity than other subtypes, suggesting that immunotherapy is more suitable for patients with TNBC (21). However, several recent clinical trials indicated that the current immunotherapy strategies (for example, anti-PD-1 or anti-PD-L1 antibody) had low efficacy in the whole population of patients with TNBC as a result of limited or extensive infiltration of immune cells or immunosuppressive cells, respectively, in the TMEs (22,23). In other words, most of patients with TNBC fail to respond to current immunotherapies because of the 'non-inflamed' or 'cold' immune microenvironments and transforming immune-cold tumor into immune-hot tumor may be a promising solution to this challenge (22,24). In the present study, 4T1 BC cells, a poorly immunogenic triple-negative model, were selected as the primary tumor model (25,26). SHK was wrapped into methoxy poly(ethylene glycol)-b-poly(ε-caprolactone-co-1,4,8-trioxa[4.6]spiro-9-undecanone) (mPECT) nanoparticles and loaded with mPECT-modified gold nanorods (AuNRs) in a supramolecular hydrogel for intratumoral injection to realize the combination of mild PTT and SHK local tumor treatment (Fig. 1A). Mild PTT triggered immune activation rapidly in the immunosuppressive microenvironment, while SHK strongly induced ICD and persistently inhibited the activation of IDO1 and expression of PD-L1 induced by mild PTT. The combination of these two treatments formed a synergistic effect to turn immune 'cold' tumor into 'hot' tumor, thereby enhancing a strong and long-lasting antitumor immunity and suppressing untreated distant tumors (Fig. 1B). The present study demonstrates the potential of low-dose local SHK administration to induce systemic antitumor immunity and provides a preclinical framework for the further development of localized SHK-based combination strategies in immune-cold TNBC.

Materials and methods

Chemicals and reagents. Shikonin (SHK, >98% purity) was obtained from Yuanye Biotechnology (https://www.shyuanye.com/). Cyclodextrin (α-CD), cetyltrimethyl ammonium

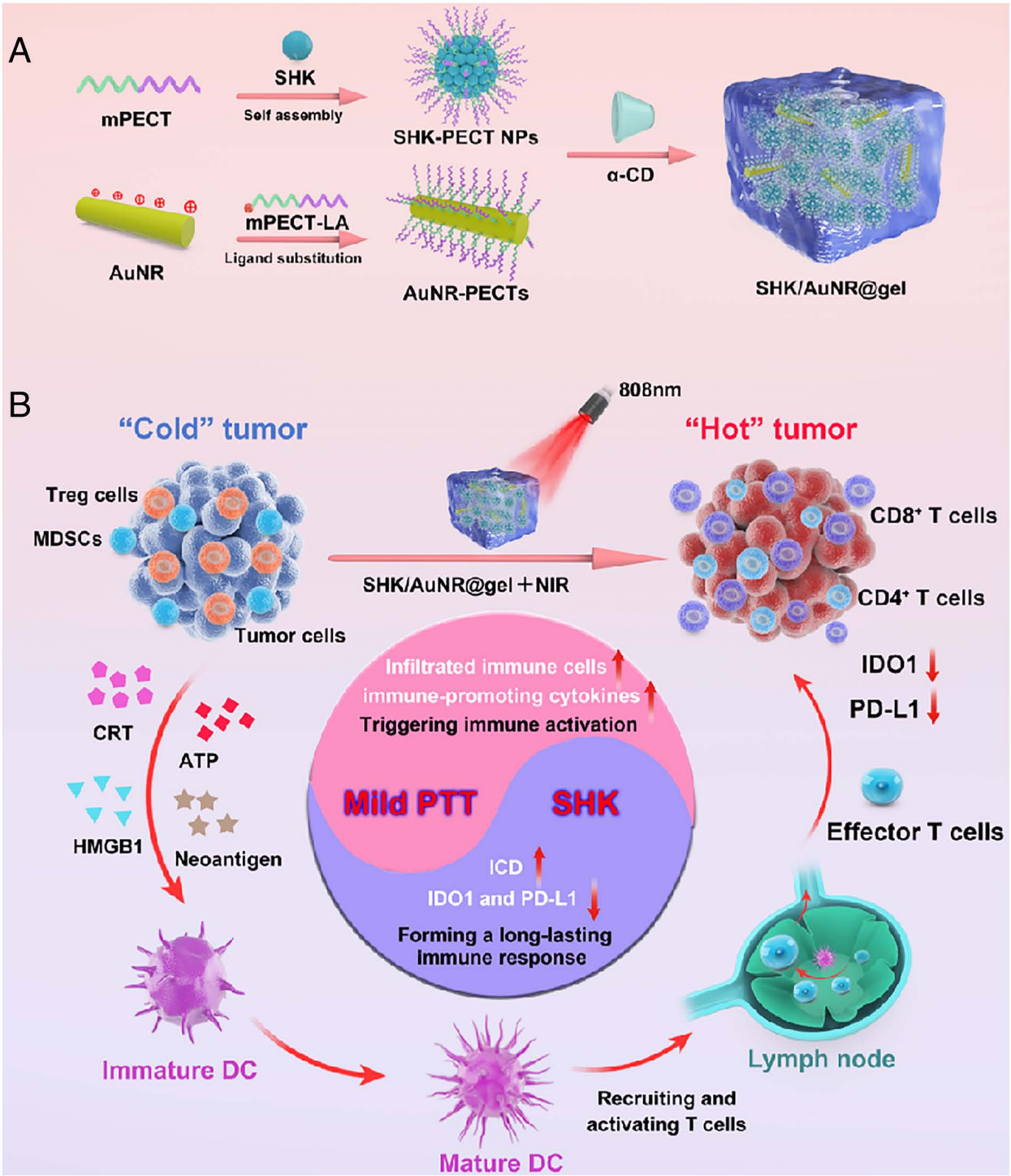

Figure 1. Schematic diagram for the preparation and function of SHK/AuNR@gel. (A) Preparation of SHK/AuNR@gel. (B) The mechanism of SHK/AuNR@gel in tumor tissues. Briefly, mild PTT increases the infiltration of immune cells into tumors, upregulates the expression of immune-promoting cytokines, and triggers the immune activation rapidly in tumor immunosuppressive microenvironment. SHK strongly induces ICD and persistently inhibits the activation of IDO1 and expression of PD-L1 induced by mild PTT. The combination of these two forms a synergistic effect to turn immune 'cold' tumor into 'hot' tumor, enhance antitumor immunity and attack the metastatic tumors. SHK, shikonin; AuNRs, gold nanorods; PTT, photothermal therapy; ICD, immunogenic cell death; PD-L1, programmed death-ligand 1; IDO1, indoleamine 2,3-dioxygenase 1; HMGB1, high mobility group box 1; CRT, calreticulin; DC, dendritic cell.

bromide (CTAB) and sodium borohydride ($NaBH_4$) were supplied by Shanghai Aladdin Biochemical Technology Co., Ltd. 4-(dimethylamino) pyridine (DMAP), N,N-dicyclohexyl carbodiimide (DCC), lipoic acid, tetrachloroauric acid (HAuCl4·4H2O), ascorbic acid and silver nitrate (AgNO3) were obtained from MilliporeSigma. Diethyl ether, tetrahydrofuran (THF), dimethyl-sulfoxide (DMSO) and hydrochloric acid were obtained from Nantong Jiangtian Chemical Co., Ltd. 3-[4,5-dimethylthiazol-2-yl]-2,5-diphenyltetrazolium bromide (MTT) was supplied by Beyotime Institute of Biotechnology. Cell culture reagents were purchased from Gibco; Thermo Fisher Scientific, Inc.).

Cell lines and animals. Two TNBC cell lines (murine TNBC cells 4T1 and human TNBC cells MDA-MB-231) were supplied by the Chinese Academy of Sciences and cultured in RPMI-1640 (4T1 cells) or DMEM (MDA-MB-231 cells) containing 10% (vol/vol) FBS (Gibco; Thermo Fisher Scientific, Inc.) and 1% penicillin/streptomycin (Thermo Fisher Scientific, Inc.) at 5% CO_2 and 37˚C as previously described (27).

BALB/c mice (female, 6-8 weeks old, weighing 18-20 g) were supplied by Vital River Laboratories. All mice were maintained under specific pathogen-free conditions in an individually ventilated cage facility with a 12/12-h dark/light cycle at 23˚C and had *ad libitum* access to water and food. Animals were monitored at least once daily throughout the study. Predefined humane endpoints were strictly implemented, and every effort was made to minimize pain, distress, and suffering. All animal procedures were conducted in accordance with the Guidelines for Care and Use of Laboratory Animals of Air Force Medical University and were approved by the Animal Ethics Committee of Air Force Medical University (approval no. 20241327; Xi'an China). The study design and animal welfare measures were conducted in accordance with internationally recognized principles for animal research and widely accepted welfare guidelines for oncology studies involving laboratory animals (28-30). A total of 220 mice were used across all *in vivo* experiments. The bilateral tumor (abscopal) model and the long-term immune memory/rechallenge studies were performed using independent cohorts of animals.

Animal welfare, tumor monitoring, anesthesia, blood collection and euthanasia. Animals were assessed at least once daily for general health and well-being, including activity, posture, grooming behavior, food and water intake, and signs of pain or distress. Tumor growth was monitored every 3 days by palpation and caliper measurements, while body weight was recorded daily. Tumor volume was calculated using the formula: 0.5 x length x width^2.

Humane endpoints were defined *a priori*. Mice were euthanized if any of the following criteria were met: i) Tumor ulceration, necrosis, bleeding or infection; ii) impaired mobility or inability to access food or water; iii) body weight loss of ≥20% from baseline; or iv) excessive tumor burden, defined as any single tumor exceeding 2,000 mm^3 in volume.

For near-infrared irradiation (NIR) and surgical procedures, including tumor resection and tissue collection, mice were anesthetized with inhaled isoflurane (3-4% for induction and 1-2% for maintenance in oxygen) and placed on a warming pad. Local tumor temperature during irradiation was continuously monitored using an infrared thermometer or thermal imaging camera.

For pharmacokinetic analysis, 150 μl of blood was collected from the tail vein at each sampling time point. Independent cohorts of mice were used for each time point, and no animal underwent more than two tail-vein blood collections within a 24-h period. For hematological and serum biochemical analyses, whole blood (500-800 μl per mouse) was collected once at the experimental endpoint as a terminal procedure via cardiac puncture under deep isoflurane anesthesia (4-5% for induction, 2-3% for maintenance in oxygen until loss of the pedal withdrawal reflex), immediately followed by euthanasia and tissue collection.

For euthanasia, mice were deeply anesthetized with inhaled isoflurane (4-5% for induction, 2-3% for maintenance in oxygen) until complete loss of the pedal withdrawal reflex, followed by cervical dislocation. Death was confirmed by the absence of respiration, heartbeat, and reflex responses before necropsy and tissue harvesting.

Preparation of SHK-loaded mPECT nanoparticles (SHK-mPECTs) and mPECT-modified gold nanorods (AuNR-mPECTs). The mPECT diblock copolymers were prepared via ring-opening polymerization of 1,4,8-trioxa [4.6] spiro-9-undecanone (TOSUO) and ε-caprolactone at 130˚C using mPEG as an initiator (31). SHK could be encapsulated in the mPECT cores via a hydrophobic interaction, and SHK-mPECT nanoparticles were prepared using the nanoprecipitation approach (32,33). Briefly, mPECT (200 mg) and SHK (2 mg) were dissolved in 2 ml THF, which was added dropwise to 20 ml deionized water under constant stirring. After removing THF through vaporization for 24 h, the SHK-mPECTs were produced by lyophilization (33).

Gold nanorods (AuNRs) were prepared using a facile, seedless synthesis method (34). Briefly, 150 μl cold $NaBH_4$ (0.01 M), 700 μl ascorbic acid (78.8 mM), 80 μl HCl (37%) and 2.5 ml $AgNO_3$ (4 mM) were added to a mixture solution (100 ml) of 0.2 M CTAB and 1 mM $HAuCl_4$ (33). After stirring at 30˚C for 6 h, the obtained AuNR-CTAB solution was kept at room temperature overnight. The AuNR-CTAB solution was purified via centrifugation (11,100 x g, 15 min) and rinsed twice before reaction to eliminate residual CTAB coating. Lipoic acid (LA)-modified mPECT (LA-mPECT) was prepared as previously described by the authors (33). Briefly, 0.137 g LA and 0.413 g DCC were dissolved in 1 ml DCM and then stirred for 12 h. Next, 1 g mPECT and 0.12 g DMAP in 10 ml DCM was added. After stirring under nitrogen at 35˚C for another 48 h, the mixture was precipitated in cold ether and vacuum-dried at 25˚C. AuNR-mPECTs were prepared by dropwise addition of 2 ml LA-mPECT solution (10 mg/ml) in DMSO to a dispersion of 100 ml AuNRs (0.01 mg/ml) under vigorous stirring, followed by an overnight incubation. After recovery of AuNR-mPECTs via centrifugation (16,600 x g, 15 min) and washing twice with deionized water, the mixture was ultimately dispersed in water to the final concentration of 100 μg/ml.

Preparation of hydrogels with different loadings. For the preparation of empty mPECT hydrogel, 60 mg α-CD was added to 1 ml of empty mPECT NPs [200 mg/ml, prepared via nanoprecipitation (35)], and then stirred vigorously until the formation of a hydrogel.

For the preparation of SHK@gel (C_{SHK}=2 mg/ml, C_{mPECT}=200 mg/ml, $C_{\alpha\text{-}CD}$=60 mg/ml), 60 mg α-CD was added to 1 ml of SHK-mPECTs solution (200 mg/ml) and then stirred vigorously until the formation of a hydrogel.

For the preparation of AuNR@gel (C_{AuNR}=50 μg/ml, C_{mPECT}=200 mg/ml, $C_{\alpha\text{-}CD}$=60 mg/ml), 200 mg lyophilized powder of empty mPECT NPs was dispersed in 1 ml AuNR-mPECTs solution (50 μg/ml) and then added with 60 mg α-CD under stirring.

To prepare SHK/AuNR@gel (C_{SHK}=2 mg/ml, C_{AuNR}=50 μg/ml, C_{mPECT}=200 mg/ml, $C_{\alpha\text{-}CD}$=60 mg/ml), 60 mg α-CD was added to an AuNR-mPECTs solution (1 ml, 50 μg/ml) containing 200 mg lyophilized powder of SHK-mPECTs. Finally, the mixture was stirred vigorously until the formation of a nano-composite hydrogel.

Characterization. TU-1900 spectrophotometer (Purkinje General Instrument) was used to collect UV-Vis spectra. The fluorescence spectral data were recorded using a fluorescence spectrophotometer (Agilent) at 520 nm. The zeta potential and hydrodynamic size of the nanoparticles were determined by dynamic light scattering (DLS; Nano ZS90; Malvern Instruments, Ltd.) at 25˚C. The concentration of AuNRs was measured by ICP-MS (7700x; Agilent, Technologies, Inc.). JEOL 100CXII transmission microscope (accelerating voltage=100 kV) was utilized to obtain transmission electron microscopy (TEM) images. The inner morphology of the obtained hydrogel was examined by S-4800 field-emission scanning electron microscopy (SEM; Hitachi, Ltd.). Rheological measurement of the hydrogel was conducted using a fluid rheometer (MCR 302; Anton Paar, Austria). An infrared thermal camera (I5; FLIR, USA) was used to monitor the temperatures of the hydrogel and AuNR solution. To investigate the degradation and SHK content in SHK/AuNR@gel, 500 μl hydrogel was placed in a 10-ml test tube and then added with 5 ml PBS (pH 7.4). At regular intervals, the supernatant (3 ml) was collected, lyophilized and dissolved in DMF. The SHK levels were examined using the UV-Vis spectrophotometer.

Investigation of the inhibitory effect of IDO1. As described previously (11), the 4T1 cells or MDA-MB-231 cells ($5x10^5$ cells/well) were cultured in a 6-well plate. On the following day, the cells were transfected with pcDNA3.1-mIDO1 or pcDNA3.1-hIDO1 (Synbio Technologies) using Lipofectamine 2000 (Invitrogen; Thermo Fisher Scientific, Inc.). After transfection for 24 h, the cells ($2.5x10^4$ cells/well) were cultured in a 96-well plate and treated with the indicated agents for 24 h. Then, the culture medium (200 μl) was mixed with 30% trichloroacetic acid (100 μl; MilliporeSigma). After incubation at 65˚C for 15 min and centrifugation (12,000 r/min, 10 min), the supernatant (100 μl) was mixed with 2% (w/v) p-dimethyl-amino-benzaldehyde (100 μl; D2004; MilliporeSigma) in acetic acid. SpectraMax Plus 384 microplate reader (Molecular Devices, LLC) was used to measure the yellow-colored kynurenine at 492 nm.

Luciferase assay. The cells were seeded in 48-well plates at a density of $3x10^4$ cells/well and cultured under normal conditions for 24 h. Subsequently, the cells were transfected with 0.2 μg pNFκB-luc (Beyotime Institute of Biotechnology) and 0.01 μg pRL-TK Renilla (Beyotime Institute of Biotechnology) using Lipofectamine 2000 for 24 h and then treated with different concentrations of SHK for another 24 h. After treatment, the cells were lysed using passive lysis buffer, and the luciferase activity was detected using a Dual Luciferase Reporter kit (Beyotime Institute of Biotechnology) (36). The experiment was carried out in triplicate and repeated three times independently.

Western blot analysis. As described previously (37), the total protein or nuclear protein was isolated using RIPA buffer (Thermo Fisher Scientific, Inc.) or nuclear and cytoplasmic protein extraction kit (cat. no. P0027; Beyotime Institute of Biotechnology), respectively. The protein concentrations were evaluated using a BCA protein assay kit. After separation through 10% SDS-PAGE, the protein samples (30 μg per lane) were transferred onto PVDF membranes (Wuhan Servicebio Technology Co., Ltd.). The membranes were blocked in 5% non-fat milk for 60 min, and then exposed to primary antibodies overnight at 4˚C. The following antibodies were employed: Anti-PD-L1 (1:1,000; cat. no. GB115704; Wuhan Servicebio Technology Co., Ltd.), anti-NF-κB p65 (1:1,000; cat. no. GB12142; Wuhan Servicebio Technology Co., Ltd.), anti-Histone H3 antibody (1:1,000; cat. no. GB11102; Wuhan Servicebio Technology Co., Ltd.) and anti-β-actin antibody (1:1,000; cat. no. AF7018; Affinity Biosciences). After rinsing, the membranes were exposed to anti-mouse or anti-rabbit HRP-labeled secondary antibodies (1:5,000; cat. nos. SA00001-1 and SA00001-2, respectively; Proteintech Group, Inc.) for 1 h. The protein blots were visualized by ECL reagent (MilliporeSigma). Semi-quantitative densitometry analysis of protein expression was performed using ImageJ v1.46r (National Institutes of Health). Band intensities of target proteins were normalized to the corresponding loading controls and expressed relative to the corresponding control group.

Assessment of ICD. To assess treatment-induced ICD *in vitro*, 4T1 or MDA-MB-231 cells were seeded in flat-bottom 96-well plates at a density of $1x10^4$ cells per well and allowed to adhere overnight. Cells were then treated for 24 h with various concentrations of free SHK or the indicated nano-formulations, with or without NIR irradiation, at equivalent SHK concentrations. Following treatment, cells were gently washed three times with PBS and fixed in 4% paraformaldehyde (PFA) for 10 min at room temperature without permeabilization to restrict antibody binding to cell-surface calreticulin (CRT). The cells were then blocked with 5% bovine serum albumin (BSA; cat. no. ST023; Beyotime Institute of Biotechnology) in PBS for 1 h and incubated with rabbit anti-CRT primary antibody (cat. no. ab227444; Abcam; 1:200 dilution in 1% BSA/PBS) for 2 h. After three washes with PBS, cells were incubated with HRP-conjugated goat anti-rabbit IgG secondary antibody (Proteintech Group, Inc.; 1:5,000 dilution in 1% BSA/PBS) for 1 h at room temperature. After extensive washing, 3,3',5,5'-tetramethylbenzidine substrate was added, and color development was allowed to proceed in the dark for 10-15 min before termination with 2 M H_2SO_4. Absorbance was measured at 450 nm using a microplate reader. Meanwhile, cell viability in replicate wells subjected to identical treatments was assessed by the MTT assay. CRT signals were normalized to the corresponding MTT absorbance values at 570 nm to account for differences in viable cell numbers and expressed as fold-change relative to untreated controls.

In addition, culture supernatants were collected after treatment and centrifuged to remove cellular debris prior to further analysis. The concentrations of ATP and HMGB1 were determined using a commercial ATP Determination Kit (cat. no. S0027) and HMGB1 ELISA Kit (cat. no. PH406;

both from Beyotime Institute of Biotechnology), respectively, according to the manufacturers' instructions.

Evaluation of cytotoxicity. The viability of cells was assessed by MTT assay as described previously (37,38). Briefly, the cells were cultured in a 96-well plate at 37˚C for 24 h. Then, MTT (5 mg/ml) was added (20 μl/well) and incubated for another 4 h. After eliminating the supernatant, the formazan crystals were dissolved in DMSO (150 μl/well). The absorbance was measured using an ELX 800 microplate reader (BioTek; Agilent Technologies, Inc.) at 570 nm.

Caspase-3/7 activity assay. Caspase-3/7 activity was measured using the Caspase-Glo® 3/7 Assay kit (cat. no. G8091; Promega Corporation) according to the manufacturer's instructions. Briefly, 4T1 cells were seeded into white 96-well plates and allowed to adhere overnight before treatment with free SHK at the indicated concentrations for 24 h. Following treatment, an equal volume of Caspase-Glo 3/7 reagent was added directly to each well containing cells and culture medium. Plates were gently mixed on an orbital shaker for 30 sec and incubated at room temperature in the dark for 30-60 min to allow cell lysis and substrate cleavage. Luminescence was measured using a microplate reader, and background signal from medium-only wells was subtracted. Caspase-3/7 activity for each treatment condition was normalized to that of untreated control cells and expressed as fold-change relative to control. All treatment conditions were assayed in triplicate wells, and each experiment was independently repeated at least three times.

Antitumor study of SHK/AuNR@gel on the local tumors. The left mammary fat pad of each female BALB/c mouse was orthotopically inoculated with 4T1 cells ($5x10^5$ cells suspended in 50 μl PBS). Once tumors reached ~150 mm^3, the mice were randomly assigned to 5 groups, and administered with 50 μl empty mPECT@gel, free SHK solution, SHK@gel, AuNR@gel, and SHK/AuNR@gel via intratumoral injection. Mice were anesthetized with inhaled isoflurane prior to irradiation as described above. After injection, mice in the NIR-treated groups were irradiated with an 808-nm laser under real-time temperature monitoring. The laser power was adjusted as needed to rapidly reach and maintain the local tumor temperature at ~43˚C for 15 min. This temperature-controlled photothermal stimulation was performed every other day for a total of four sessions, ending on day 6 after intratumoral injection.

Body weight (BW) was recorded daily, and tumor dimensions were measured every 3 days using calipers. Tumor volume was calculated as 0.5 x length x $width^2$. On day 8 after intratumoral administration, a portion of tumor tissue was collected under anesthesia for immune-response analysis. Mice were monitored until a single tumor exceeded 2,000 mm^3 or predefined humane endpoints were reached, and survival time was recorded.

Kynurenine (Kyn) and tryptophan (Trp) measurement in vivo. Detection of Trp and Kyn content in tumor tissues was conducted as previously described (39). Briefly, the tumor tissues were harvested from tumor-bearing mice (TBM) treated with different therapeutics for homogenization using homogenizer. After dissolving the homogenate in trichloroacetic acid (10%), the contents of Trp and Kyn in the supernatant were detected using the LC-MS system (Agilent 1290 Series LC System). Data collection and analysis were conducted with Analyst software (version 1.6.3; SCIEX). The Kyn to Trp ratio (Kyn/Trp) was employed as an indicator of IDO activity.

Immunofluorescence staining. Immunofluorescence staining was conducted as described previously (40). Briefly, freshly dissected tumor tissue was fixed in 4% PFA at 25˚C for 48 h, dehydrated through a graded ethanol series (75, 85, 90, 95 and 100% ethanol; 1 h each), embedded in paraffin wax, and sliced into 4-μm-thick sections. After permeabilization (0.1% Triton X-100; Beyotime Institute of Biotechnology), the sections were blocked for 1 h at room temperature with 10% normal donkey serum (cat. no. ANT051; Wuhan Antgene Biotech Co., Ltd.), and exposed to primary antibodies, anti-PD-L1 (aPD-L1; 1:100; cat. no. ab213480; Abcam) overnight at 4˚C. Subsequently, the sections were exposed to fluorescent secondary antibody (1:200; cat. no. sc-362281; Santa Cruz Biotechnology, Inc.) and DAPI (0.001 mg/ml; cat. no. KGA215-10; Nanjing KeyGen Biotech Co., Ltd.), the immunofluorescence image was obtained using a fluorescence microscope (EVOS FL Auto; Thermo Fisher Scientific, Inc.). Data analysis was performed with ImageJ software.

In vivo ICD analysis. Immunohistochemistry was performed to observe the markers of ICD, CRT and HMGB1, using an indirect peroxidase method (41). The paraffin-embedded tissue section was dewaxed in xylene and rehydrated in a graded series of decreasing concentrations of ethanol. After quenching endogenous peroxidase with hydrogen peroxide (3%), the section was blocked with goat serum (10%; ZSGB-Bio) for 30 min at room temperature to inhibit non-specific antibody binding. The tissue sections were incubated overnight with primary antibody at 4˚C. Antibodies against CRT (1:100; cat. no. ab227444) and HMGB1 (1:350; cat. no. ab79823) were supplied by Abcam. Subsequently, the sections were exposed to HRP-conjugated goat anti-rabbit IgG (1:200; cat. no. SA00001-2; Proteintech Group, Inc.). The chromogenic substrate used in the present study was diaminobenzidine (DAB; ZSGB-Bio). After counterstaining with hematoxylin and mounting in resin, images were obtained using an Aperio pathology scanner. The IOD values were determined with ImageJ software.

Immune-response sampling from primary tumors and tumor-draining lymph nodes. Primary tumors and ipsilateral inguinal/axillary tumor-draining lymph nodes (TDLNs) were collected 24 h after the final treatment. TDLNs were used for $CD11c^+$ dendritic cell (DC) enrichment, qPCR-based analysis of DC maturation markers, and IL-12p70 ELISA. Primary tumor tissues were used for qPCR-based assessment of T-cell infiltration- and cytolytic activity-related genes, as well as CD4/CD25-enriched Foxp3 analysis.

Magnetic enrichment of immune cell subsets. $CD11c^+$ cells were isolated from TDLNs using positive magnetic selection with CD11c MicroBeads UltraPure (mouse; cat. no. 130-125-835; Miltenyi Biotec, Inc.) and LS Columns (cat.

no. 130-042-401; Miltenyi Biotec, Inc.). $CD4^+$ tumor-infiltrating lymphocytes (TILs) were enriched from tumor tissues using the Tumor Dissociation Kit (mouse; cat. no. 130-096-730; Miltenyi Biotec, Inc.), CD4 (TIL) MicroBeads (mouse; cat. no. 130-116-475; Miltenyi Biotec, Inc.), and LS Columns. Where indicated, CD25 surface labeling-based magnetic enrichment was further performed using mouse CD25 MicroBeads (cat. no. 130-091-072; Miltenyi Biotec, Inc.), and RNA was extracted from the CD25-enriched $CD4^+$ fraction for Foxp3 analysis. For *ex vivo* memory T-cell assays, splenic $CD8^+$ T cells were purified by negative selection using the MojoSort™ Mouse $CD8^+$ T Cell Isolation Kit (cat. no. 480008; BioLegend, Inc.), whereas $CD11c^+$ DCs were enriched using CD11c MicroBeads (Miltenyi Biotec, 130-108-338).

RT-qPCR analysis. Total RNA was extracted from cells, tumor tissues, or enriched immune cell fractions using TRIzol™ reagent (cat. no. 15596026; Thermo Fisher Scientific, Inc.), the RNeasy Micro Kit (cat. no. 74004; Qiagen China Co., Ltd.), or the RNeasy Mini Kit (cat. no. 74104; Qiagen), as appropriate. RNA was reverse-transcribed into cDNA using PrimeScript™ RT Master Mix (cat. no. RR036A; Takara) or PrimeScript™ RT Reagent Kit (cat. no. RR037A; Takara Biotechnology Co., Ltd.). RT-qPCR was performed on a CFX96 Real-Time PCR System using TB Green® Premix Ex Taq™ II (cat. no. RR820A; Takara) under the following thermocycling conditions: Initial denaturation at 95˚C for 30 sec, followed by 40 cycles of denaturation at 95˚C for 5 sec and annealing/extension at 60˚C for 30 sec. GAPDH was used as the reference gene, and relative expression was calculated using the $2^{-\Delta\Delta Cq}$ method (42). For DC maturation analysis, H2-Ab1, Cd80, Cd86, Il12a and Il12b were quantified in $CD11c^+$ cells isolated from TDLNs, and the DC maturation index was calculated as the mean z-score of the normalized expression values of these five genes (43). The primer sequences for RT-qPCR were as follows: GAPDH forward, 5'-CATCACTGCCACCCAGAAGACTG-3' and reverse, 5'-ATGCCAGTGAGCTTCCCGTTCAG-3'; H2-Ab1 forward, 5'-GTGTGCAGACACAACTACGAGG-3' and reverse, 5'-CTGTCACTGAGCAGACCAGAGT-3'; Cd80 forward, 5'-CCTCAAGTTTCCATGTCCAAGGC-3' and reverse, 5'-GAGGAGAGTTGTAACGGCAAGG-3'; Cd86 forward, 5'-ACGTATTGGAAGGAGATTACAGCT-3' and reverse, 5'-TCTGTCAGCGTTACTATCCCGC-3'; Il12a forward, 5'-CTGTGCCTTGGTAGCATCTATG-3' and reverse, 5'-GCAGAGTCTCGCCATTATGATTC-3'; Il12b forward, 5'-TGGTTTGCCATCGTTTTGCTG-3' and reverse, 5'-ACAGGTGAGGTTCACTGTTTCT-3'; Cd3e forward, 5'-GCTCCAGGATTTCTCGGAAGTC-3' and reverse, 5'-ATGGCTACTGCTGTCAGGTCCA-3'; Cd4 forward, 5'-GTTCAGGACAGCGACTTCTGGA-3' and reverse, 5'-GAAGGAGAACTCCGCTGACTCT-3'; Cd8a forward, 5'-ACTACCAAGCCAGTGCTGCGAA-3' and reverse, 5'-ATCACAGGCGAAGTCCAATCCG-3'; Gzmb forward, 5'-CAGGAGAAGACCCAGCAAGTCA-3' and reverse, 5'-CTCACAGCTCTAGTCCTCTTGG-3'; Prf1 forward, 5'-TTTCGCCTGGTACAAAAACC-3' and reverse, 5'-CGTTCAGGCAGTCTCCTACC-3'; Foxp3 forward, 5'-CCCAGGAAAGACAGCAACCTT-3' and reverse, 5'-TTCTCACAACCAGGCCACTTG-3'; Tnf forward, 5'-CCCTCACACTCAGATCATCTTCT-3' and reverse, 5'-GCTACGACGTGGGCTACAG-3'; Ifng forward, 5'-GCCACGGCACAGTCATTGA-3' and reverse, 5'-TGCTGATGGCCTGATTGTCTT-3'; and Cd274 forward, 5'-TGCGGACTACAAGCGAATCACG-3' and reverse, 5'-CTCAGCTTCTGGATAACCCTCG-3.

ELISA and ELISpot assays. IL-12p70 levels in TDLN homogenates were quantified using a Mouse IL-12p70 ELISA Kit (cat. no. 88-7121-22; Invitrogen; Thermo Fisher Scientific, Inc.) and normalized to total protein content (44). For *ex vivo* memory immune-response analysis, granzyme B and perforin concentrations were quantified using Mouse Granzyme B ELISA (cat. no. MBS2507805; MyBioSource, Inc.) and Mouse Perforin ELISA (cat. no. MBS2021832; MyBioSource, Inc.) kits, respectively. IFN-γ, TNF-α, IL-2, CXCL9 and CXCL10 levels in culture supernatants were measured using the corresponding commercial ELISA kits according to the manufacturers' instructions. IFN-γ-producing T cells were quantified using a Mouse IFN-γ ELISpot Kit (cat. no. 552569; BD Biosciences), and results were expressed as spot-forming units (SFU) per 10^5 T cells. Polyfunctional T cells simultaneously producing IFN-γ and TNF-α were quantified using a Dual-Color Mouse ELISpot Kit (cat. no. SPOT-09-2; Mabtech), and results were expressed as double-positive SFU per 10^5 T cells.

Calculation of intratumoral immune indices. For T-cell infiltration analysis, Cd3e, Cd8a and Cd4 were quantified in tumor tissues, and the T-cell infiltration index was calculated as the mean z-score of normalized Cd3e, Cd8a and Cd4 expression values (45). Cytolytic activity (CYT) was quantified by the average of the log-transformed expression values of Gzmb and Prf1, corresponding to the geometric mean of their expression on a linear scale (46). Foxp3 expression was quantified in CD25-enriched $CD4^+$ TILs and normalized to the corresponding control group (47).

Detection of SHK concentration in vivo. To measure SHK levels in plasma and tumor tissues, 4T1 TBM were intratumorally injected with free SHK, SHK@gel, or SHK/AuNR@gel. The treatment schedule was identical to that used in the local tumor therapy study described above. Peripheral blood (150 μl per mouse per time point) was collected from the tail vein at predetermined time points into heparinized tubes. Independent cohorts of mice were used for each sampling time point. Plasma was obtained by centrifugation at 850 x g for 10 min, transferred to clean polypropylene tubes and stored at -80˚C until analysis. To determine SHK content in plasma, 50 μl plasma samples were mixed with 200 μl ethyl acetate, followed by vortexing (10 min) and centrifugation (15,000 rpm, 10 min, 4˚C). The obtained SHK solution was dried through evaporation and reconstituted in 100 μl 50% methanol /50% acetonitrile containing 1% formic acid (48). To detect SHK content in tumors, the tumor tissues were homogenized in saline (ratio of tumor weight-to-volume=1:1), and the protein was precipitated with 5 volume of 50% methanol/50% acetonitrile containing 1% formic acid. After centrifugation (21,100 x g, 5 min, 4˚C), the supernatant was filtered using a 0.22-μm filter, and subsequently analyzed with the HPLC system (Shimadzu LC-20AT).

Safety evaluation of the therapies. At the terminal time point, whole blood (500-800 μl per mouse) was collected by cardiac puncture under deep anesthesia for hematological and serum biochemical analyses, followed immediately by euthanasia as aforementioned. Hematology and serum biochemistry were analyzed by the Clinical Laboratory of Xijing Hospital, including hepatorenal function markers [blood urea nitrogen (BUN), creatinine (CREAT), alkaline phosphatase (ALP), alanine aminotransferase (ALT) and aspartate aminotransferase (AST)] and routine blood parameters [monocyte (Mono), lymphocyte (LYMPH), hematocrit (HCT), hemoglobin (HGB), platelet (PLT), red blood cell (RBC) and white blood cell (WBC) counts]. Major organs were collected, fixed in 4% neutral-buffered PFA, and assessed by H&E staining. BW was recorded throughout the experiment.

Bilateral tumor model and T-cell depletion. For the bilateral tumor model, $5x10^5$ 4T1 cells suspended in 50 μl PBS were injected into the right mammary fat pad to establish the primary tumor. Three days later, an equal number of 4T1 cells was injected into the contralateral mammary fat pad to establish the distant tumor, following a previously reported short-interval bilateral orthotopic tumor model (49). When the primary tumor volume reached ~150 mm^3, mice were randomly assigned to five treatment groups and received intratumoral injections (50 μl) of empty mPECT@gel, free SHK solution, SHK@gel, AuNR@gel + NIR, or SHK/AuNR@gel + NIR. Mice were anesthetized with inhaled isoflurane prior to NIR irradiation and surgical procedures, as described above. NIR irradiation was performed using the same temperature-controlled protocol described above. After completion of the treatment schedule, the primary tumor was surgically resected. BW was monitored daily, and the volume of untreated contralateral tumors was measured every 3 days. Immune-related molecular endpoints in distant tumors, including T-cell infiltration-related genes, cytolytic effector genes and Foxp3 expression in CD25-enriched $CD4^+$ TILs, were analyzed using the same magnetic enrichment, RT-qPCR and calculation procedures described above.

For depletion of $CD4^+$ and $CD8^+$ T cells, bilateral tumor-bearing mice were intraperitoneally injected with anti-CD8 antibody (10 mg/kg; BioXcell, clone 53-6.7) or anti-CD4 antibody (10 mg/kg; BioXcell, clone GK1.5), with the corresponding IgG isotype controls (BioXcell, BE0089 or BE0090), once every 3 days starting from the implantation of the distant tumor (50). Intratumoral administration and NIR irradiation were performed as described above. BW was monitored daily, and distant tumor growth was assessed every 3 days. The bilateral tumor model was conducted in accordance with the same animal monitoring and humane endpoint criteria described above (28-30,51).

Tumor rechallenge and experimental lung metastasis models. Female BALB/c mice were orthotopically inoculated with 4T1 cells ($5x10^5$ cells per mouse in 100 μl PBS) into the mammary fat pad. When tumors reached ~150 mm^3, mice were randomly assigned into five treatment groups and received intratumoral injections (50 μl) of blank mPECT@gel, free SHK solution, SHK@gel, AuNR@gel + NIR, or SHK/AuNR@gel + NIR. For the NIR-treated groups, tumors were irradiated using the same temperature-controlled 808-nm laser protocol described above. Two days after the final treatment, primary tumors were surgically resected under anesthesia to simulate complete local tumor eradication.

On day 30 after treatment, mice were rechallenged subcutaneously with 4T1 cells ($5x10^5$ cells per mouse) in the contralateral flank to evaluate systemic antitumor immune memory (52,53). Rechallenge tumor growth was monitored every 3 days by caliper measurements, and tumor volume was calculated as 0.5 x length x $width^2$. In a separate cohort, mice received intravenous injection of $1x10^5$ 4T1 cells on day 30 after treatment to establish an experimental lung metastasis model. Fourteen days later, mice were euthanized, and lungs were harvested, rinsed with PBS and fixed in 4% PFA. Surface metastatic nodules were counted under a dissecting microscope (S9D; Leica Microsystems GmbH), and lung tissues were processed for H&E staining to assess pulmonary micrometastasis. Animal monitoring and humane endpoints were applied as aforementioned.

Ex vivo functional analysis of memory T cells. To characterize memory immune responses, spleens were harvested on day 31 after treatment. Single-cell suspensions were prepared by mechanical dissociation, filtration through 70-μm cell strainers and erythrocyte lysis. Purified $CD8^+$ T cells and enriched $CD11c^+$ DCs were prepared as described in the magnetic enrichment of immune cell subsets section. DCs were pulsed with 4T1 tumor lysates (100 μg/ml protein) for 3 h at 37˚C and washed three times to remove free antigen. Purified $CD8^+$ T cells were then co-cultured with antigen-loaded DCs at an E:T ratio of 10:1 for antigen-specific recall assays.

The frequency of IFN-γ-producing T cells and IFN-γ/TNF-α double-positive T cells was measured by ELISpot as described in the ELISA and ELISpot assays section. Cytotoxic activity of memory $CD8^+$ T cells was evaluated using a colorimetric lactate dehydrogenase (LDH) cytotoxicity assay kit (cat. no. 88953; Thermo Fisher Scientific, Inc.). Effector $CD8^+$ T cells were co-incubated with 4T1 target cells at E:T ratios of 5:1, 10:1, 20:1 and 40:1 for 6 h, followed by absorbance measurement at 490 nm. Specific lysis was calculated as [(sample-spontaneous)/(maximum-spontaneous)] x100%, and overall cytotoxic activity was summarized as the area under the dose-response curve using GraphPad Prism v9.0.

For molecular profiling, total RNA was extracted from purified $CD8^+$ T cells and analyzed by RT-qPCR as aforementioned. For degranulation analysis, $CD8^+$ T cells were co-cultured with antigen-pulsed DCs for 4 h, after which culture supernatants and cell lysates were collected separately. Degranulation capacity was calculated as [supernatant/(supernatant + lysate)] x100% based on granzyme B and perforin levels, and the mean release rate of these two markers was used as an overall measure of cytotoxic granule exocytosis. Recall cytokine responses were assessed by co-culturing T cells with antigen-pulsed DCs for 48 h, followed by ELISA-based measurement of IFN-γ, TNF-α, IL-2, CXCL9 and CXCL10 as aforementioned.

Statistical analysis. All data are presented as the mean ± SD. Statistical tests were performed using SPSS Statistics version 31.0 (IBM Corp.). The differences among the groups were

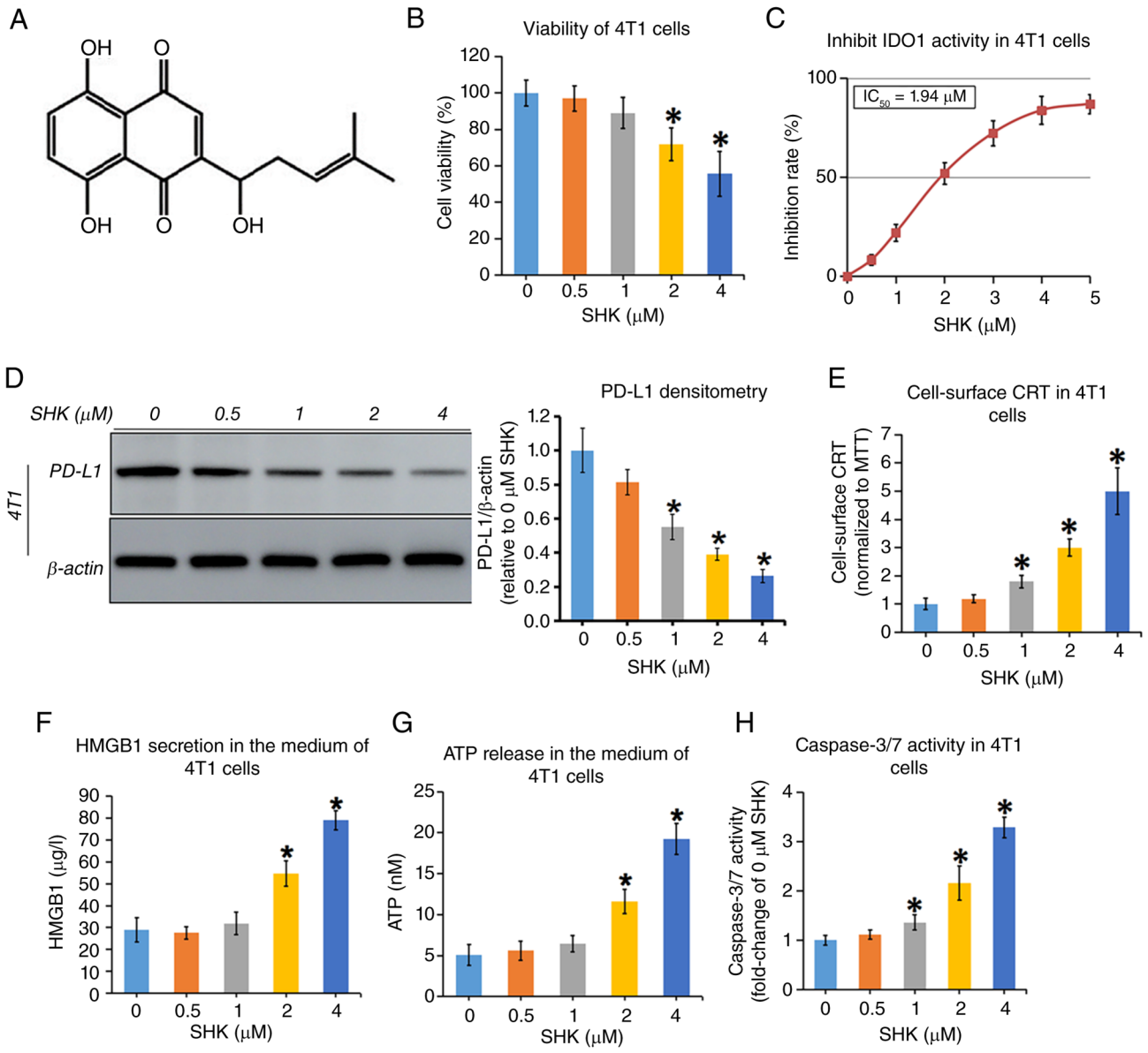

Figure 2. *In vitro* effects of different concentrations of free SHK on cell viability, IDO1 activity, PD-L1 expression and ICD-associated damage signals in 4T1 cells. (A) The chemical structure of SHK. (B) Cell viability of 4T1 cells treated with increasing concentrations of free SHK for 24 h, as determined by the MTT assay and expressed as percentage of the 0 μM SHK group. (C and D) Inhibitory effects of SHK at different concentrations on IDO1 catalytic activity (C) and PD-L1 expression (D) in 4T1 cells. (E) CRT levels in 4T1 cells after 24 h treatment with SHK, quantified by a cell-based ELISA under non-permeabilizing conditions and normalized to cell viability. (F and G) Extracellular HMGB1 (F) and ATP (G) levels in culture supernatants of SHK-treated 4T1 cells. (H) Caspase-3/7 activity in 4T1 cells after 24 h exposure to SHK, expressed as fold-change relative to the 0 μM SHK group. Data are presented as the mean ± SD (n=3 independent experiments). *P<0.05 vs. 0 μM SHK. SHK, shikonin; IDO1, indoleamine 2,3-dioxygenase 1; PD-L1, programmed death-ligand 1; ICD, immunogenic cell death; CRT, calreticulin; HMGB1, high mobility group box.

compared by one-way ANOVA and Bonferroni's post-hoc test. The intergroup survival rates were determined using the log-rank test of Kaplan-Meier survival curves. P<0.05 was considered to indicate a statistically significant difference.

Results

Free SHK inhibits IDO1 catalytic activity and PD-L1 expression and induces ICD-like responses in TNBC cells. Increasing evidence indicates that indoleamine 2,3-dioxygenase 1 (IDO1) plays a vital role in modulating tumor immune evasion, with IDO1-associated depletion of tryptophan and accumulation of toxic metabolites frequently observed in immunosuppressive TMEs (54). SHK, a naphthoquinone compound (Fig. 2A), has been reported to exert a notable inhibitory effect on the catalytic activity of IDO1 (11). Consistent with these observations, the concentration-dependent effects of free SHK were first examined in 4T1 cells. Exposure to SHK for 24 h resulted in a gradual reduction in cell viability, with only minimal effects observed at 0.5-1 μM and moderate cytotoxicity at 2-4 μM, where more than 50% of cells remained viable (Fig. 2B). Within this concentration range, SHK inhibited IDO1 enzymatic activity in a dose-dependent manner, yielding an IC_{50} value of ~1.94 μM (Fig. 2C), consistent with a previous study (11). Notably, 1 μM SHK produced

only low-to-moderate inhibition of IDO1 activity, whereas inhibition approaching 50% was mainly observed at ~2 μM. Programmed death-ligand 1 (PD-L1), another critical mediator of tumor-associated immunosuppression (55), was likewise downregulated by SHK in a concentration-dependent manner (Fig. 2D). Previous studies, including one by the authors, have demonstrated that SHK suppresses nuclear factor-κB (NF-κB) signaling in multiple experimental settings (38,56,57). In agreement with these findings, SHK significantly reduced NF-κB transcriptional activity, as assessed using an NF-κB-responsive luciferase reporter assay, and inhibited nuclear translocation of NF-κB p65 in 4T1 cells (Fig. S1A and B). Given the established role of NF-κB in promoting PD-L1 transcription (58), these results suggest that inhibition of the NF-κB pathway may contribute, at least in part, to the SHK-mediated downregulation of PD-L1. ICD is characterized by the release or exposure of DAMPs that facilitate antigen uptake and promote DC maturation (59). To determine whether SHK induces ICD-related signals in TNBC cells within the aforementioned concentration range, several canonical DAMPs and cell-death-associated parameters were quantified in 4T1 cells. Under non-permeabilizing conditions, SHK induced a concentration-dependent increase in normalized cell-surface CRT exposure, as determined by cell-based ELISA after normalization to viable cell number (Fig. 2E). Consistent with the induction of ICD, extracellular HMGB1 and ATP levels in culture supernatants were significantly elevated following treatment with 2 and 4 μM SHK (Fig. 2F and G). Moreover, caspase-3/7 activity increased in a concentration-dependent manner, with pronounced elevations observed at 1-4 μM (Fig. 2H), indicating engagement of apoptotic signaling pathways within this moderately cytotoxic concentration range. To determine whether these effects extended beyond murine TNBC, parallel studies were performed in human MDA-MB-231 cells. As revealed in Fig. S2A-F, SHK similarly reduced cell viability, suppressed IDO1 activity and PD-L1 expression, and enhanced cell-surface CRT exposure as well as HMGB1 and ATP release in a concentration-dependent manner. Collectively, these findings demonstrate that, at concentrations causing only partial loss of viability, SHK simultaneously inhibits IDO1 catalytic activity and PD-L1 expression, while promoting the release of hallmark ICD-associated DAMPs in both murine and human TNBC cells, consistent with the induction of an immunostimulatory ICD-like cell-death program.

Preparation and characterization of AuNR-mPECTs and SHK-mPECTs. In the present study, AuNRs were prepared using the seedless synthesis method (34), and AuNR-mPECTs were synthesized through the 'ligand substitution method' based on the authors' previous procedures (33). Compared with AuNRs, AuNR-mPECTs exhibited a similar characteristic UV-Vis absorption, as revealed by longitudinal and transverse plasmonic peaks at 785 and 520 nm, respectively (Fig. 3A). The longitudinal plasmonic peak was slightly red-shifted, which might correspond to the surface modification of mPECTs. Dynamic light scattering showed a dominant hydrodynamic size peak at 50 nm (PDI=0.642) for AuNRs and 58 nm (PDI=0.449) for AuNR-mPECTs (Fig. 3B). The decreased zeta potential and increased particle size of AuNR-mPECTs confirmed the successful substitution of positively charged CTAB on the surface of AuNR-mPECTs (Fig. 3B and C). The micro-morphology of AuNR-mPECTs was examined by TEM. Notably, AuNR-mPECTs showed a typical rod structure, with the long and short diameters of 48±8 and 11±2 nm, respectively (Fig. 3D). The stability of AuNR-mPECTs is critical for their biomedical applications. To validate their dispersion stability under physiological conditions (osmotic pressure, protein and the microenvironment of acid-base abnormalities in tumors), AuNR-mPECTs were dispersed in 10% FBS-containing culture medium, NaCl solution (0.1 M) and PBS solution (pH 7.4 or 6.8), respectively. After 24 h of incubation, the UV-Vis spectral data of all samples were obtained, and similar longitudinal and transverse absorption peaks were observed in each spectrogram (Fig. S3A), indicating its optical stability in different media. Furthermore, the stability of AuNR-mPECTs was evaluated by measuring hydrodynamic diameter after exposure to various media mimicking the *in vivo* microenvironment. It was found that the hydrodynamic diameter of AuNR-mPECTs showed no obvious changes after incubation with different media (Fig. S3B). Furthermore, the UV-Vis spectral data or particle size of AuNR-mPECTs had no significant changes after laser irradiation, suggsting the excellent photothermal stability of AuNR-mPECTs (Fig. S3C and D). Additionally, no significant changes were observed in UV-Vis spectral data and particle size after 10 days of storage, indicating AuNR-mPECTs have favorable storage stability (Fig. S3E and F). In addition to the aforementioned results, the surface coating with mPECTs could greatly reduce the toxicity of AuNRs, and no significant cytotoxicity of AuNR-mPECTs was observed, even at 50 μg/ml (Fig. S4A and B).

SHK, which is a hydrophobic drug, can be encapsulated in the hydrophobic core of mPECT nanoparticles through hydrophobic interaction to form drug-loaded SHK-mPECT nanoparticles (SHK-mPECTs). TEM images showed that SHK-mPECTs had a uniform spherical structure (Fig. 3E). The hydrodynamic diameter of SHK-mPECTs was ~141 nm with a narrow distribution (PDI=0.262) (Fig. 3F). Fluorescence and UV-Vis absorption characterization revealed that loading SHK into nanoparticles did not affect the optical properties of SHK compared with bare SHK at the same concentration, suggesting that the loading of SHK into nanoparticles did not affect the chemical properties of SHK (Fig. 3G and H). Moreover, the effects of different nano-components on IDO1 activity, PD-L1 expression and ICD induction were further assessed. As demonstrated in Fig. 3I-M, compared with free SHK, SHK-mPECTs showed the same or even slightly stronger effects on inhibiting IDO1 activity (Fig. 3I), downregulating PD-L1 expression (Fig. 3J) and inducing ICD (Fig. 3K-M). Mild PTT stimulation significantly increased IDO1 activity and PD-L1 expression (Fig. 3I and J), but the ability of mild PTT to induce ICD was weak (Fig. 3K-M). However, the combination of mild PTT with SHK-mPECTs significantly reversed the increases in IDO1 activity and PD-L1 expression induced by mild PTT and strongly induced ICD in 4T1 cells (Fig. 3I-M). Similar trends were also detected in human TNBC MDA-MB-231 cells (Fig. S5A-E). To further exclude

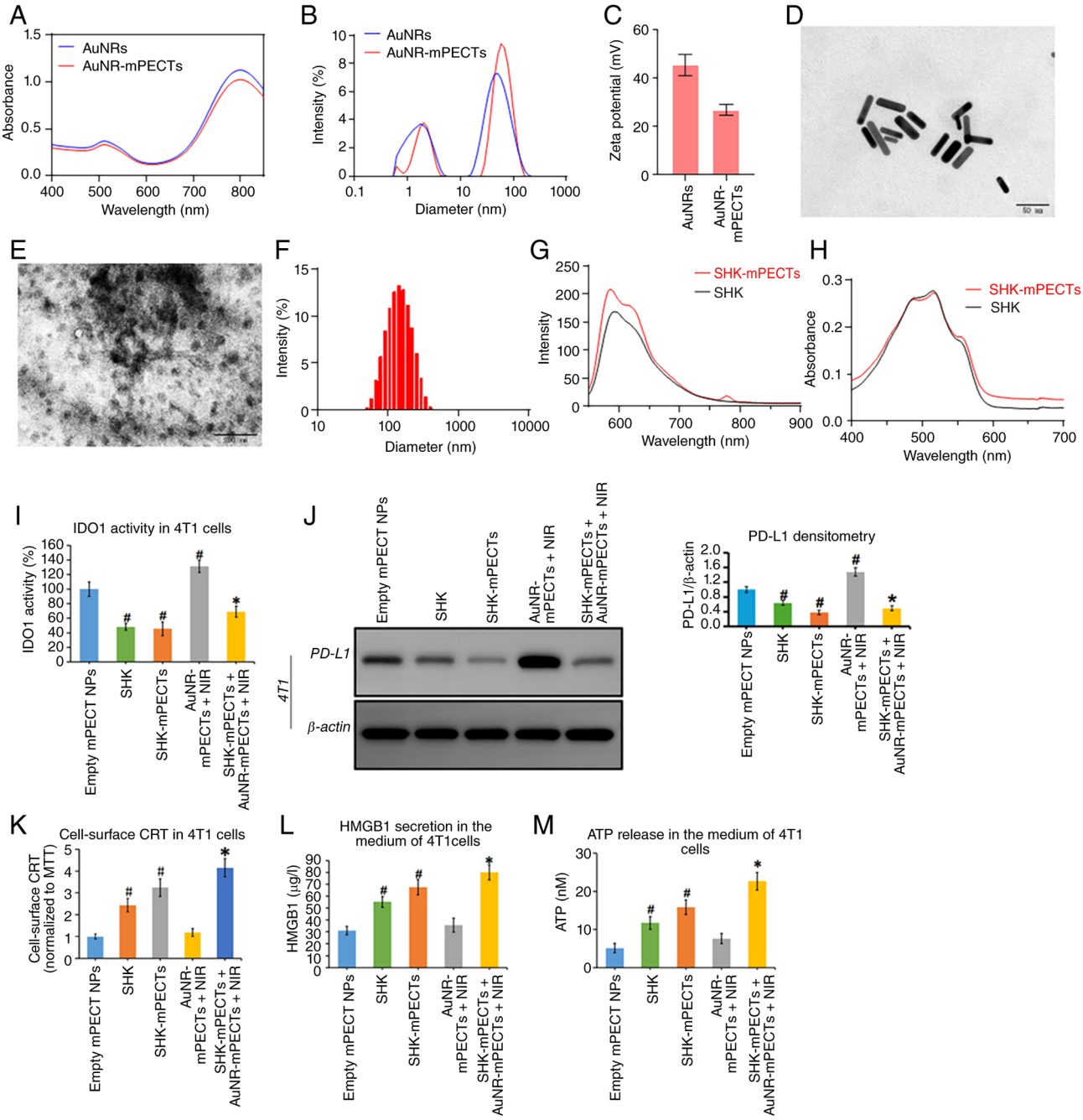

Figure 3. (A-D) UV-Vis absorption spectra (A), intensity-weighted hydrodynamic size distributions (dynamic light scattering) (B), zeta potentials (C) and TEM images (D) of AuNR-mPECTs. (E-H) TEM image (E), size and distributions (F), fluorescence spectrum (G) and UV-Vis absorption spectrum (H) of SHK-mPECTs. (I-M) The 4T1 cells were treated with free SHK (2 μM), SHK-mPECTs (the concentration of loaded SHK is equal to 2 μM), mild PTT (43˚C, 15 min) generated by AuNR-mPECTs (50 μg/ml) under NIR irradiation (808 nm, heating power: 1.5 W/cm^2, maintaining power: 0.5 W/cm^2), or SHK-mPECTs combined with AuNR-mPECTs + NIR-induced mild PTT (43˚C, 15 min). After 24 h of continuous culture, IDO1 activity (I), PD-L1 expression (J), cell-surface CRT levels (K), HMGB1 secretion (L), and ATP release into the supernatant (M) were determined in each treatment group. Mean ± SD. $^{\#}$P<0.05 vs. empty mPECT-NPs CON group, *P<0.05 vs. AuNR-mPECTs + NIR group. TEM, transmission electron microscopy; AuNRs, gold nanorods; PTT, photothermal therapy; CRT, calreticulin; HMGB1, high mobility group box.

the potential effects of the blank nanocarrier and NIR irradiation itself, a focused two-group control experiment was performed in 4T1 cells. Empty mPECT-NPs + NIR caused only a slight temperature increase and did not generate controllable mild photothermal heating. In addition, compared with empty mPECT-NPs, empty mPECT-NPs + NIR did not significantly alter IDO1 activity, PD-L1 mRNA expression, or ICD-associated markers, including CRT, HMGB1 and ATP (Fig. S6A-F).

Preparation and characterization of the nano-composite hydrogel co-constructed with AuNR@mPECTs and SHK@mPECTs (SHK/AuNR@gel). After adding α-CD into AuNR-mPECTs and SHK-mPECTs, the mixture solution was converted into a claret-red homogeneous hydrogel at the macroscopic level (Fig. 4A). A homogeneous network structure was obviously observed in the SEM images of SHK/AuNR@gel (Fig. 4B). The rheological properties of SHK/AuNR@gel were evaluated subsequently. As shown in

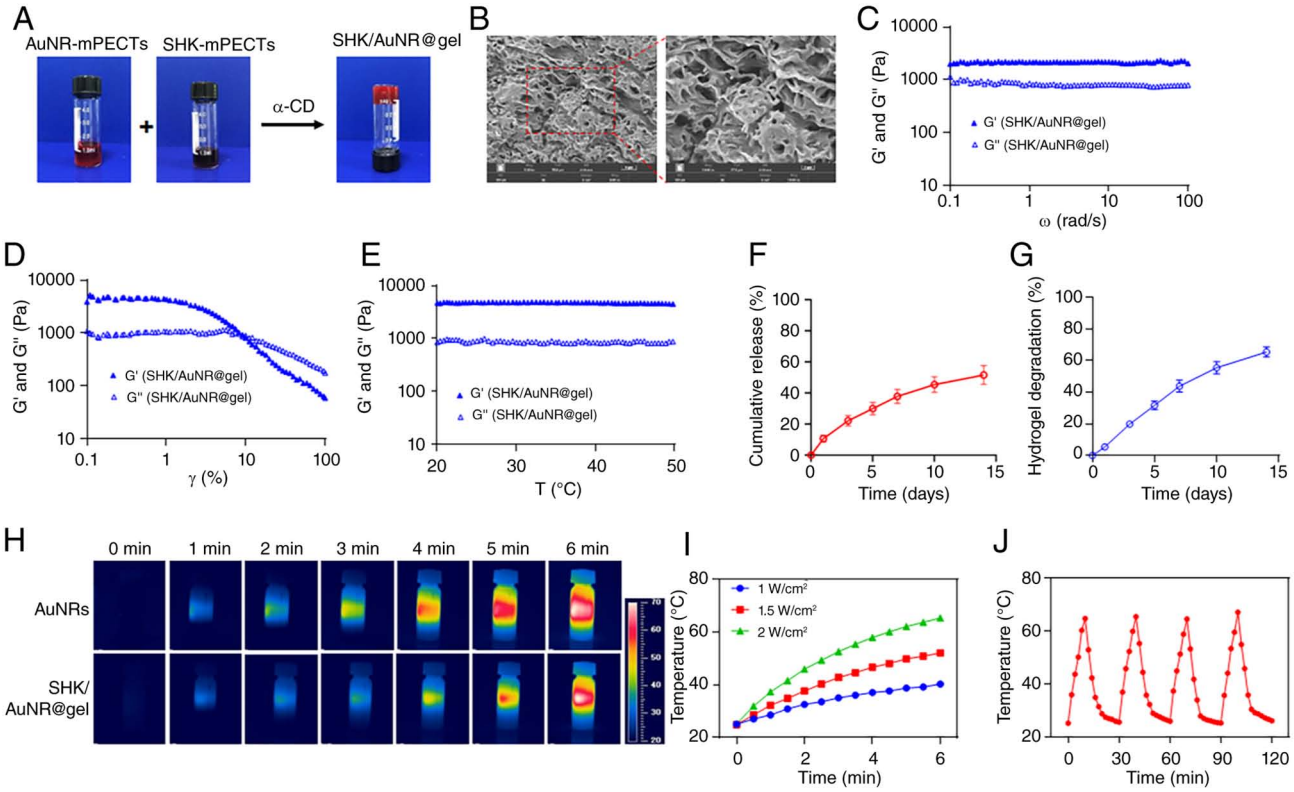

Figure 4. (A) Photo illustration of the preparation of SHK/AuNR@gel through mixing AuNR@mPECTs and SHK@mPECTs nanoparticles with α-CD (C_{AuNR}=50 μg/ml, C_{SHK}=2 mg/ml, C_{mPECT}=200 mg/ml, $C_{\alpha\text{-}CD}$=60 mg/ml). (B) Scanning electron microscopy images of SHK/AuNR@gel. (C) Modulus-angular frequency relationships of SHK/AuNR@gel. (D) Thixotropy of SHK/AuNR@gel. (E) Changes in the modulus of SHK/AuNR@gel with increasing temperatures (20-50˚C). (F) The *in vitro* SHK release and (G) SHK/AuNR@gel degradation profile. (H) Infrared thermal images of AuNRs solution and SHK/AuNR@gel (with equivalent AuNRs concentration of 50 μg/ml) under laser irradiation (808 nm, 2 W/cm^2, 6 min). (I) Temperature rise curves of SHK/AuNR@gel under different irradiation powers (2.0, 1.5, 1.0 W/cm^2) for 6 min. (J) Temperature increases of SHK/AuNR@gel during 4 successive cycles of laser irradiation for 10 min at 2.0 W/cm^2. SHK, shikonin; AuNRs, gold nanorods.

Fig. 4C, although the angular frequency was increased, the storage modulus G' of SHK/AuNR@gel was always higher than the loss modulus G', suggesting that an elastic solid-like hydrogel might be formed. Shear thinning is an essential property for realizing the injectability of a hydrogel. As revealed in Fig. 4D, with the increase of the shear strain, SHK/AuNR@gel exhibited a non-Newtonian shear thinning (pseudoplastic) behavior, which indicated that SHK/AuNR@gel was injectable. During the photothermal process, the stability is crucial for avoiding the unnecessary burst release of drugs loaded in the hydrogel at the higher treatment temperatures. As demonstrated in Fig. 4E, with the rising temperatures, the storage modulus G' of SHK/AuNR@gel was always higher than the loss modulus G', suggesting that SHK/AuNR@gel could maintain a stable gelling state at a relatively higher treatment temperature (≤50˚C). In addition, the particle size distribution of SHK-mPECTs was similar within the temperature range of 25-60˚C, suggesting that SHK-mPECT NPs could remain stable without disassembly or aggregation during hyperthermia treatment (Fig. S7). Subsequently, the release behaviors of SHK from SHK/AuNR@gel were investigated. Notably, the release of SHK in SHK/AuNR@gel showed a zero-order release curve with no obvious burst release phenomenon (Fig. 4F), indicating that SHK/AuNR@gel could maintain a controlled, sustainable release behavior. Furthermore, the degradation curve of SHK/AuNR@gel was similar to the release curve of SHK, suggesting that the release of SHK mainly depended on the dissolution and degradation of SHK/AuNR@gel (Fig. 4F and G).

Photothermal conversion efficiency (PCE) is important for the application of hydrogels in PTT. As demonstrated in Fig. 4H, the temperature of AuNRs and SHK/AuNR@gel both rose rapidly to ~60˚C within only 6 min under the irradiation of 808 nm NIR, indicating that loading AuNRs into SHK/AuNR@gel did not obviously affect the PCE of AuNRs. The photothermal conversion properties of SHK/AuNR@gel were highly dependent on the irradiated power of the laser (Fig. 4I). In other words, the higher the power irradiated on SHK/AuNR@gel, the faster the temperature rose. To explore the stability of photothermal conversion, SHK/AuNR@gel was irradiated with an 808 nm laser for 10 min at 2.0 W/cm^2 and then cooled to room temperature; this laser on/off process involved a total of 4 cycles. As demonstrated in Fig. 4J, the peak temperatures did not drop significantly during the whole process, suggesting that SHK/AuNR@gel had favorable stability of photothermal conversion even after the long-term and repeated laser irradiation. Altogether, these results indicate that SHK/AuNR@gel has excellent efficiency and stability for photothermal conversion.

Antitumor effect of SHK/AuNR@gel + NIR treatment on local tumors. Based on previous studies (25,26), BALB/c

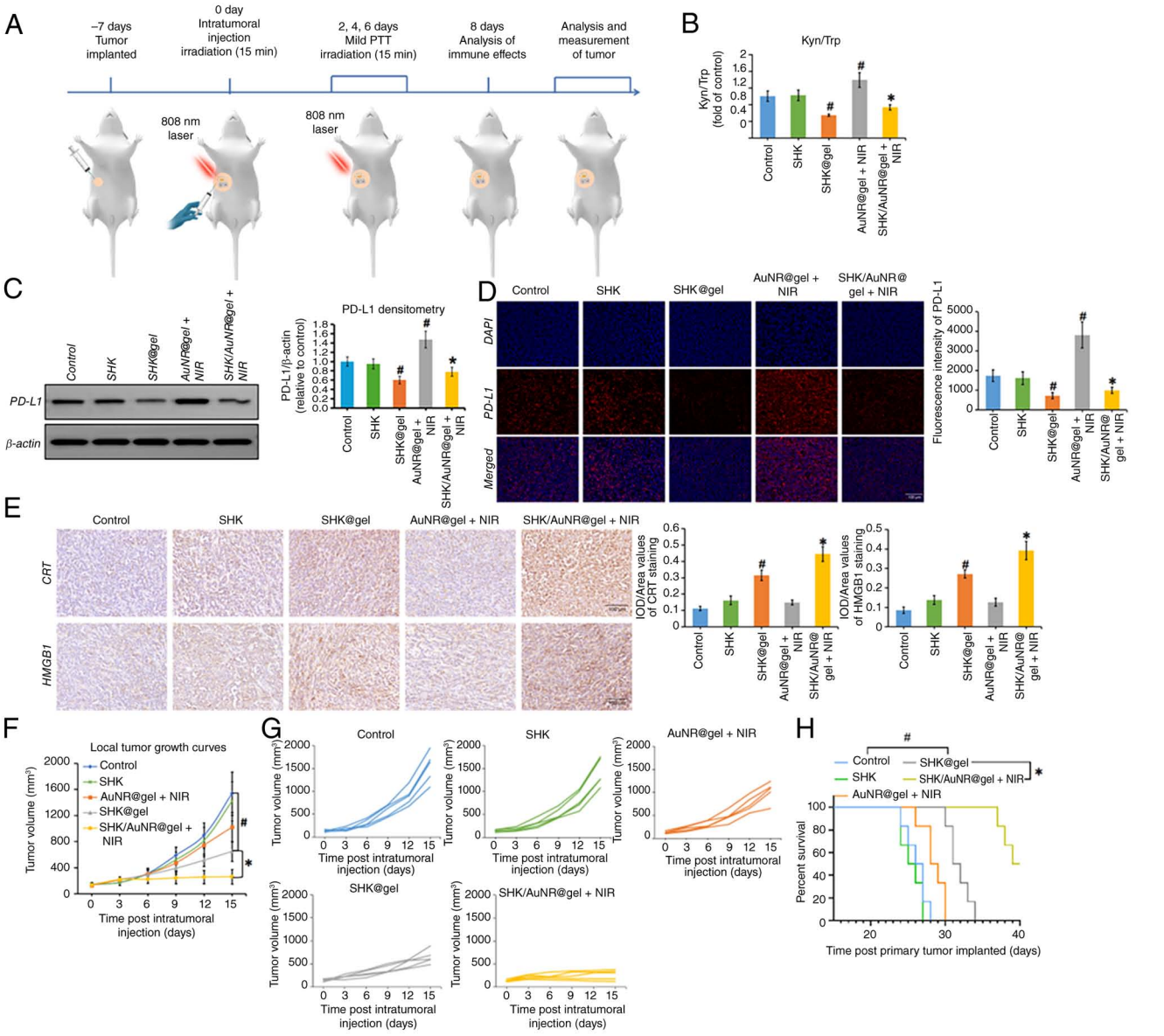

Figure 5. Antitumor effects of SHK/AuNR@gel + NIR on the local tumors. (A) Schematic illustration of the study design. (B) Kyn/Trp ratio in the local tumor tissue after different treatments (n=4). (C and D) The protein expression of PD-L1 was determined by western blotting (C, n=3) and immunofluorescence (D, n=3), respectively. (E) Representative Immunohistochemical images and quantification of CRT and HMGB1 positive areas in tumors (IOD/area value, n=3). Mean ± SD, $^{\#}$P<0.05 vs. Control group, *P<0.05 vs. AuNR@gel + NIR group. (F) Local TGCs with the average tumor volume in tumor-bearing mice after the indicated treatments (n=5). (G) The TGCs of each mouse in different treatment groups. (H) Survival curves of mice after the indicated treatments (n=5). Mean ± SD. $^{\#}$P<0.05 vs. Control group, *P<0.05 vs. SHK@gel group. SHK, shikonin; AuNRs, gold nanorods; NIR, near-infrared irradiation; PD-L1, programmed death-ligand; CRT, calreticulin; HMGB1, high mobility group box; TGCs, tumor growth curves.

mice bearing 4T1 tumor cells were chosen as the immune 'cold' TNBC model for *in vivo* study. To further verify the previous *in vitro* findings, the effects of hydrogel with different compositions on IDO1 activity, PD-L1 expression and ICD were first detected in local tumors. Because SHK@gel does not contain AuNRs, NIR irradiation of SHK@gel alone was not expected to generate controllable mild photothermal heating under the present experimental conditions. Therefore, SHK@gel mainly represented the effect of local sustained SHK release, whereas SHK/AuNR@gel + NIR represented the combination of hydrogel-mediated sustained SHK release and AuNR-mediated mild PTT. The detailed experimental process is shown in Fig. 5A. The activity of IDO1 could be indirectly reflected by the ratio of Kyn/Trp in tumor tissues (60). As shown in Fig. 5B-D, intratumoral injection of free SHK failed to reduce the Kyn/Trp ratio or PD-L1 expression, while the hydrogel-loaded SHK (SHK@gel) significantly reduced the ratio of Kyn/Trp (Fig. 5B) and expression of PD-L1 (Fig. 5C and D) in local tumors. It can be inferred that free SHK does not have a retention capacity after intratumoral injection, and it may quickly diffuse to the surrounding tissues or enter the systemic circulation, thus losing its direct and lasting effects on local tumors. Consistent with previous studies (18,61), the repeated stimulation of mild PTT (AuNR@gel + NIR) obviously increased the Kyn/Trp ratio and PD-L1 expression. However, the combination of mild PTT with SHK (SHK/AuNR@gel + NIR) almost completely reversed these phenomena (Fig. 5B-D). In Fig. 5E, it is

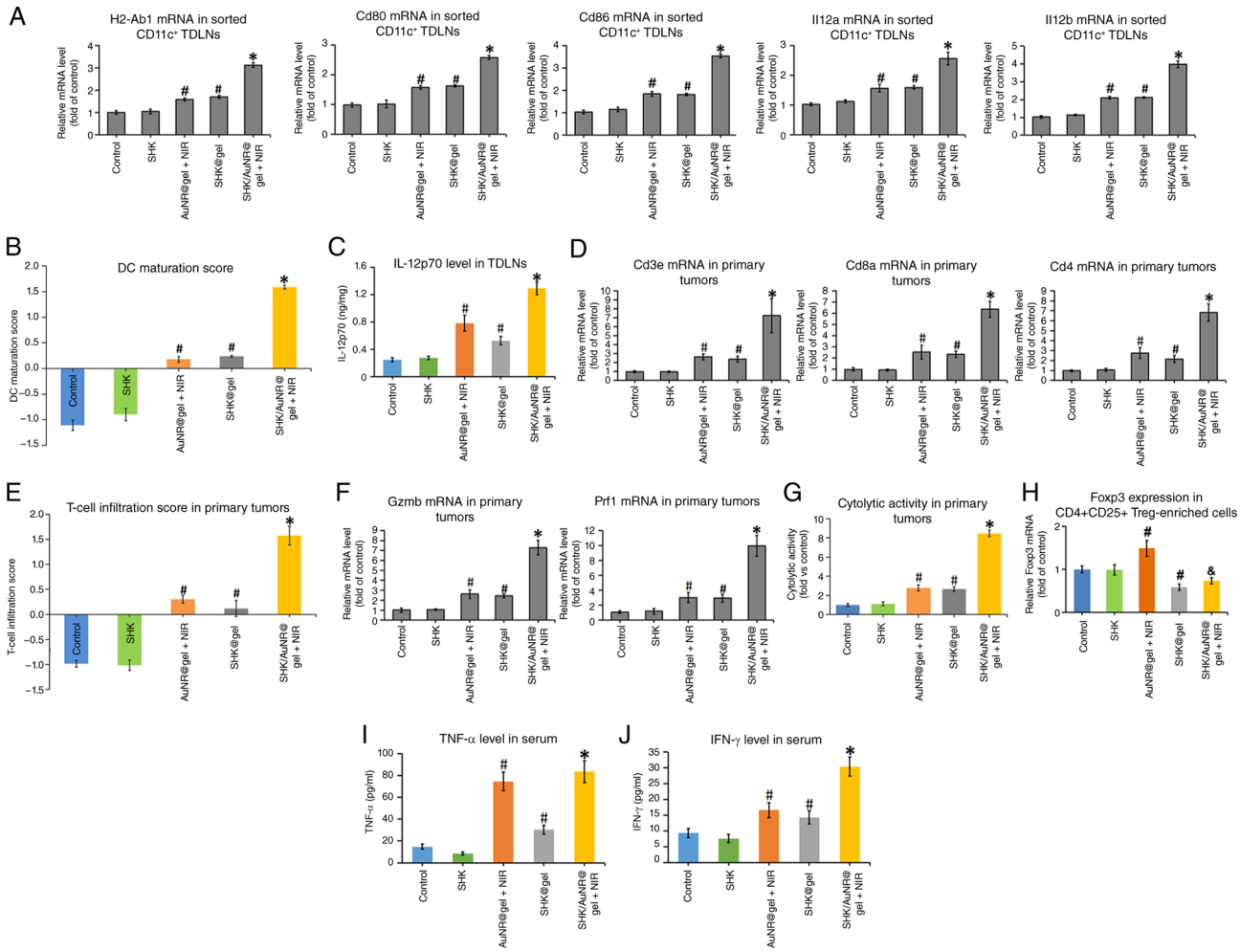

Figure 6. SHK/AuNR@gel + NIR treatment induced a strong immune response. The treatment details were given in Fig. 5A. Ipsilateral inguinal and axillary TDLNs and primary tumors were collected to quantify the immune cascade from upstream priming to intratumoral effector dominance. (A-C) DC maturation. (A) qPCR for *H2-Ab1, Cd80, Cd86, Il12a, Il12b* in sorted CD11c$^+$ TDLN cells; (B) DC maturation score (z-mean of the five markers from-ΔCt); (C) Tissue-level IL-12p70 in TDLN homogenates (ELISA; ng per mg total protein). (D-G) T-cell infiltration and CYT in primary tumors. (D) qPCR for *Cd3e, Cd8a* and *Cd4*; (E) T-cell infiltration score (z-mean of the three genes). (F) qPCR for *Gzmb* and *Prf1*; (G) CYT score (geometric mean of Gzmb/Prf1 on the log scale). (H) Foxp3 mRNA expression in CD4$^+$CD25$^+$ Treg-enriched cells magnetically enriched from primary tumor-infiltrating lymphocytes; $^{\#}$P<0.05 vs. Control; $^{\&}$P<0.05 vs. AuNR@gel + NIR. (I and J) Serum levels of TNF-α and IFN-γ after treatment for 8 days. Unless otherwise specified, data are presented as the mean ± SD (n=4 mice/group). $^{\#}$P<0.05 vs. Control group, *P<0.05 vs. SHK@gel group. SHK, shikonin; AuNRs, gold nanorods; NIR, near-infrared irradiation; TDLNs, tumor-draining lymph nodes; DC, dendritic cell; CYT, cytolytic activity.

demonstrated that the effect of AuNR@gel + NIR-mediated mild PTT on ICD induction was not obvious, while SHK@gel could significantly induce ICD, and the effect on ICD induction was further enhanced when combined with mild PTT (SHK/AuNR@gel + NIR). Furthermore, SHK/AuNR@gel + NIR almost completely inhibited the growth of the tumor (Fig. 5F and G) and significantly prolonged the survival time of tumor-bearing mice (Fig. 5H). All these results indicate that SHK/AuNR@gel + NIR not only attenuates the increases in Kyn/Trp and PD-L1 expression induced by mild PTT but also has strong abilities to induce ICD and inhibit tumor growth.

SHK/AuNR@gel + NIR treatment induces potent adaptive antitumor immunity and converts immune-cold tumors into immune-hot tumors. To characterize the antitumor immune response elicited by the hydrogel-mediated local SHK delivery combined with mild PTT, a comprehensive analysis of immune-cell activation and cytokine production was performed in TBM (Fig. 6). Within TDLNs, treatment with SHK/AuNR@gel + NIR significantly increased the DC maturation score, defined as the mean z-score of *H2-Ab1*, *Cd80*, *Cd86*, *Il12a* and *Il12b* expression levels (Fig. 6A and B). This finding indicates enhanced antigen-presenting capacity and improved priming of Th1-oriented immune responses (43,44). Consistent with the pivotal role of IL-12 in promoting Th1 differentiation and IFN-γ production (44), IL-12p70 levels in TDLN homogenates were also significantly elevated following SHK/AuNR@gel + NIR treatment (Fig. 6C).

Analysis of the primary tumors revealed a pronounced increase in T-cell infiltration in the SHK/AuNR@gel + NIR group, as reflected by a significantly higher T-cell infiltration index based on the combined expression of *Cd3e*, *Cd8a* and *Cd4* (Fig. 6D and E) (45). Moreover, the CYT score, calculated as the geometric mean of *Gzmb* and *Prf1* expression on a logarithmic scale, was substantially increased (Fig. 6F and G) (46), indicating enhanced effector T-cell functionality within the

TME. To further assess Treg-associated immunosuppressive features, $CD4^+$ TILs were first enriched from primary tumor tissues, followed by CD25 surface labeling-based magnetic enrichment and Foxp3 qPCR analysis (62). AuNR@gel + NIR treatment increased Foxp3 expression in the $CD4^+CD25^+$ Treg-enriched fraction, whereas SHK@gel and SHK/AuNR@gel + NIR reduced this Foxp3 signal (Fig. 6H). Together with the increased T-cell infiltration and CYT score, these findings suggest that SHK/AuNR@gel + NIR treatment promoted effector T-cell activity while attenuating CD25-enriched Foxp3-associated immunosuppressive features in the primary TME. Finally, levels of the Th1-associated cytokines TNF-α and IFN-γ were significantly elevated in both tumor tissues and serum from mice treated with SHK/AuNR@gel + NIR (Fig. S8A and B; Fig. 6I and J). These findings are indicative of a robust systemic Th1-polarized immune response (44). Taken together, these data demonstrate that SHK/AuNR@gel + NIR effectively remodels the immunosuppressive TME and instigates a potent, systemic adaptive immune response.

Evaluation of the therapy safety. Previous studies showed that SHK was injected intraperitoneally every other day for 3 weeks, and no apparent toxic effect was found at the dose of 5.0 mg/kg BW (36,63). In the present study, 5.0 mg/kg were also used as the dosage, but only once (through intratumoral injection). Free SHK, or an equivalent dose of SHK@gel (C_{SHK}=2 mg/ml, 50 μl) and SHK/AuNR@gel (C_{SHK}=2 mg/ml, C_{AuNR}=50 μg/ml, 50 μl) were intratumorally injected into the tumors. The concentrations of SHK in tumor tissues and plasma were quantified by HPLC analysis (Fig. 7A and B). As shown in Fig. 7A, after intratumoral injection, the concentration of free SHK in the tumor rapidly dropped to the trace level in a short time. On the contrary, the concentrations of SHK in the tumor of the two hydrogel groups (SHK@gel or SHK/AuNR@gel) retained at high levels for a longer time, indicating that the hydrogel could realize the sustained release of SHK and maintain a high concentration in local tumors for a long-lasting time. It should be noted that the local temperature rise mediated by NIR light has no obvious effect on the release profile of SHK from the hydrogel (SHK/AuNR@gel + NIR). After a single intratumoral injection, free SHK rapidly entered the blood circulation, resulting in a sudden increase in SHK in the blood and then a rapid decrease (Fig. 7B). On the contrary, the concentrations of SHK in the blood of the two hydrogel groups did not show this trend and constantly remained at a relatively low level. These findings indicated that the mPECT hydrogel used in the present study can achieve the sustained release of SHK, maintain a relatively high concentration of SHK in the local tumor for a long time, while preventing SHK from rushing into the blood circulation to cause potential damage to normal tissues. In addition, no abnormal changes in blood routine and hepatorenal functions were found among different treatment groups (Fig. 7C and D), and the BW of mice was also not affected during these therapies (Fig. 7E). Furthermore, H&E analysis revealed that no obvious histological damage was observed in the main organs, such as heart, liver, spleen, lung and kidney, after various treatments (Fig. 7F).

SHK/AuNR@gel + NIR induces a systemic abscopal effect against untreated distal tumors. To determine whether localized SHK/AuNR@gel + NIR therapy could generate systemic antitumor immunity, a bilateral TBM model was established, in which primary tumors were implanted in the right mammary fat pad and secondary (distant) tumors were implanted in the contralateral mammary fat pad three days later (Fig. 8A). Once the primary tumors reached ~150 mm^3, mice received intratumoral injections of the indicated formulations or SHK/AuNR@gel + NIR, followed by NIR irradiation where applicable. Notably, treatment with SHK/AuNR@gel + NIR resulted in pronounced inhibition of distal tumor growth compared with all other groups (Fig. 8B and C). To exclude the possibility that this effect was simply attributable to leakage of SHK from the treated primary tumor and subsequent systemic drug distribution, SHK concentrations in distant tumors were quantified by HPLC following a single intratumoral administration. As revealed in Fig. S9, SHK levels in untreated distant tumors remained extremely low and declined rapidly over time in all treatment groups, remaining well below concentrations associated with direct cytotoxicity. This abscopal effect was accompanied by substantial immune activation within the untreated distal tumors. qPCR analysis revealed significant upregulation of *Cd3e, Cd8a* and *Cd4* in distal tumors from the SHK/AuNR@gel + NIR group (Fig. 8D), resulting in a significantly elevated T-cell infiltration score (Fig. 8E). Similarly, expression levels of the cytolytic effector molecules *Gzmb* and *Prf1* were increased (Fig. 8F), leading to a corresponding increase in the composite CYT score (Fig. 8G). Furthermore, Treg-associated immunosuppressive features in untreated distant tumors were assessed using CD25 surface labeling-based magnetic enrichment of $CD4^+$ TILs. Similar to the primary tumors, AuNR@gel + NIR treatment increased Foxp3 expression in the $CD4^+CD25^+$ Treg-enriched fraction, whereas SHK/AuNR@gel + NIR reduced this Foxp3 signal (Fig. 8H). These findings, together with the increased T-cell infiltration and CYT score in distant tumors, support a shift toward a more favorable effector-dominant immune landscape after the combined local treatment. To functionally validate the contribution of T-cell subsets to the abscopal response, *in vivo* depletion studies were performed. Depletion of either $CD8^+$ or $CD4^+$ T cells substantially attenuated the ability of SHK/AuNR@gel + NIR treatment to control distant tumor growth (Fig. 8I), demonstrating that both T-cell populations are required for the generation of effective systemic antitumor immunity.

SHK/AuNR@gel + NIR treatment elicits potent and polyfunctional antitumor immune memory. Having established that SHK/AuNR@gel + NIR treatment could suppress both tumor rechallenge and experimental lung metastasis (Fig. 9A-C; and Fig. S10A-C), it was next sought to characterize the functional properties of the long-term immune memory generated by this therapeutic strategy. Splenic T cells were isolated from treated mice 1 day after intravenous challenge with 4T1 cells, as depicted in Fig. 9A, and subjected to a comprehensive panel of *ex vivo* functional analyses. The antigen specificity of the memory T-cell response was first evaluated. Using an IFN-γ enzyme-linked immunospot (ELISpot) assay, it was found that T cells isolated from SHK/AuNR@gel + NIR-treated mice exhibited a significantly stronger response to 4T1 tumor lysates than those

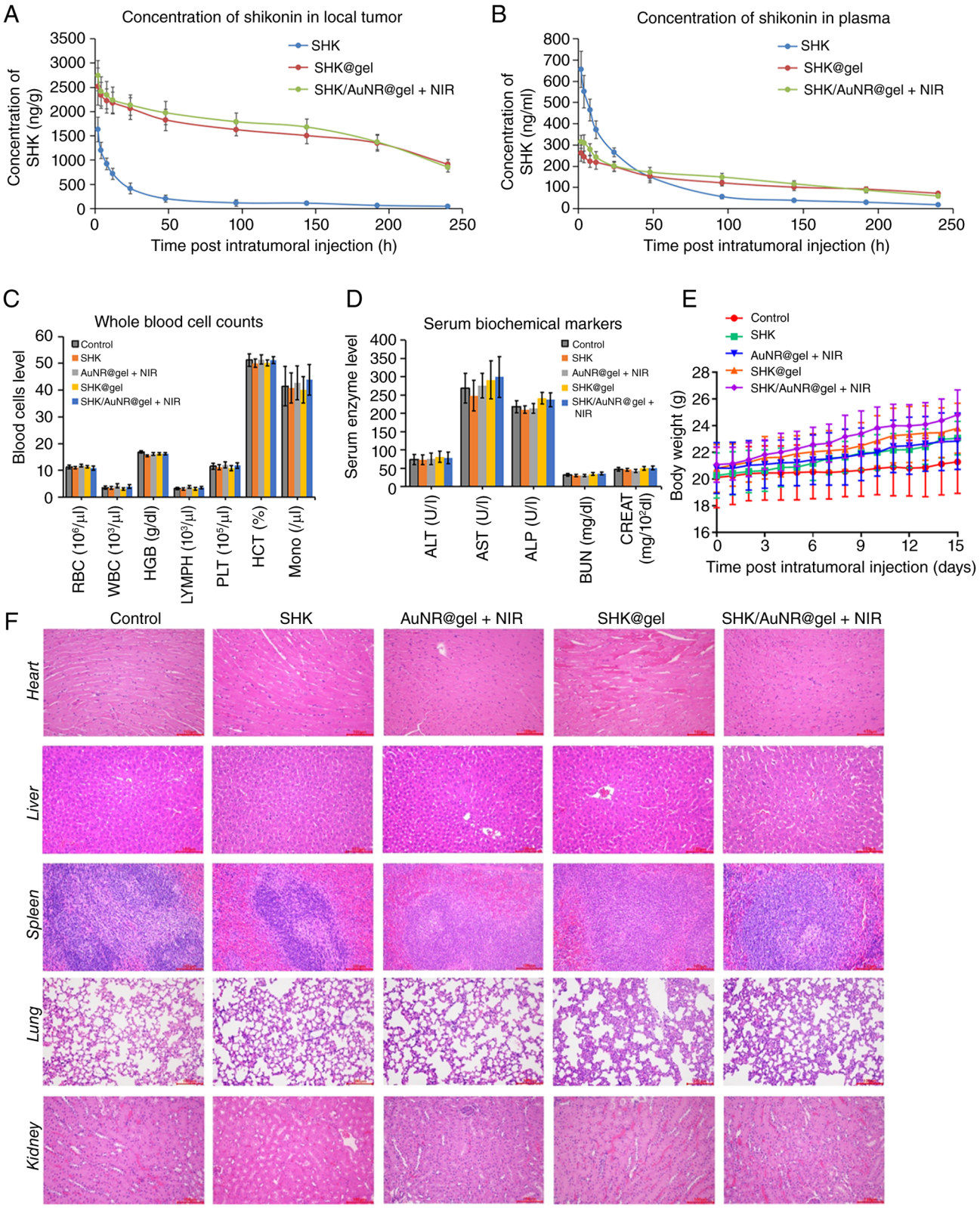

Figure 7. Biosafety evaluation *in vivo*. The treatment details are given in Fig. 5A. (A and B) HPLC analysis of SHK concentrations in tumors (A, n=3) and plasma (B, n=3) after injection with free SHK, SHK@gel, or SHK/AuNR@gel (dose of SHK is unified as 5 mg/kg BW). (C and D) Statistical analysis of whole blood cell counts (C, n=5) and serum biochemical markers (D, n=5) of TBM after various treatments. All indicators were within normal biological ranges. (E) The averaged mouse BW profile of each group during therapies (n=5). (F) Representative images of H&E morphological analysis of the main organs of TBM after the indicated treatments (Magnification, 200x; n=3). SHK, shikonin; BW, body weight; AuNRs, gold nanorods; TBM, tumor-bearing mice.

from all other treatment groups, as reflected by a significantly higher number of SFU per 10^5 T cells (Fig. 9D). The cytotoxic effector function of these memory T cells was next assessed. $CD8^+$ T cells were enriched from the splenocytes and co-cultured with irradiated 4T1 target cells at multiple effector-to-target (E:T) ratios in a short-term LDH release

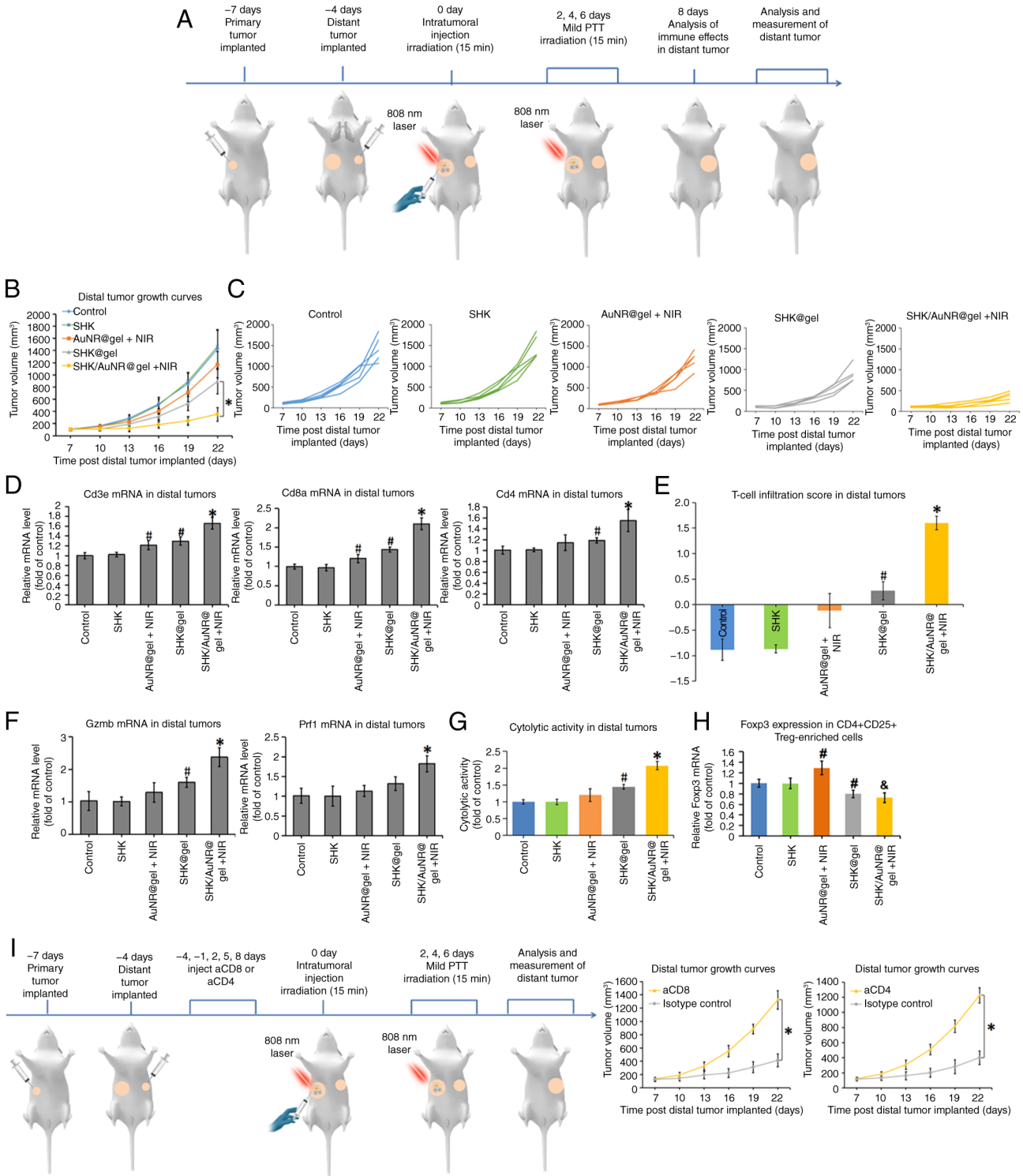

Figure 8. Abscopal effects in a bilateral tumor model *in vivo*. (A) Schematic of the bilateral design and distal tumor sampling. (B) Distal TGCs in the bilateral model (n=5 mice/group); group means shown. *P<0.05 vs. SHK@gel. (C) Individual distal TGCs for each mouse by group. (D-G) T-cell infiltration and CYT in distal tumors. (D) qPCR for Cd3e, Cd8a and Cd4. (E) T-cell infiltration score (z-mean of the three genes). (F) qPCR for Gzmb and Prf1. (G) CYT score (geometric mean of Gzmb/Prf1 on the log scale); #P<0.05 vs. Control; *P<0.05 vs. SHK@gel. (H) Foxp3 mRNA expression in $CD4^+CD25^+$ Treg-enriched cells magnetically enriched from distant tumor-infiltrating lymphocytes; #P<0.05 vs. Control; &P<0.05 vs. AuNR@gel + NIR. (I) Distal TGCs under $CD8^+$ or $CD4^+$ T-cell depletion; *P<0.05 vs. isotype control. Unless otherwise specified, data are presented as the mean ± SD (n=4 mice/group). #P<0.05 vs. Control; *P<0.05 vs. SHK@gel. TGCs, tumor growth curves; SHK, shikonin; CYT, cytolytic activity; qPCR, quantitative PCR; AuNRs, gold nanorods; NIR, near-infrared irradiation; PTT, photothermal therapy.

assay. $CD8^+$ T cells derived from the SHK/AuNR@gel + NIR group displayed potent, dose-dependent tumor cell killing across all E ratios tested. Consistent with this observation, the overall cytotoxic capacity, quantified as the area under the dose-response curve (AUC), was significantly greater than that observed in all control groups (Fig. 9E).

To further elucidate the mechanisms underlying the enhanced cytotoxic activity of memory T cells, the expression

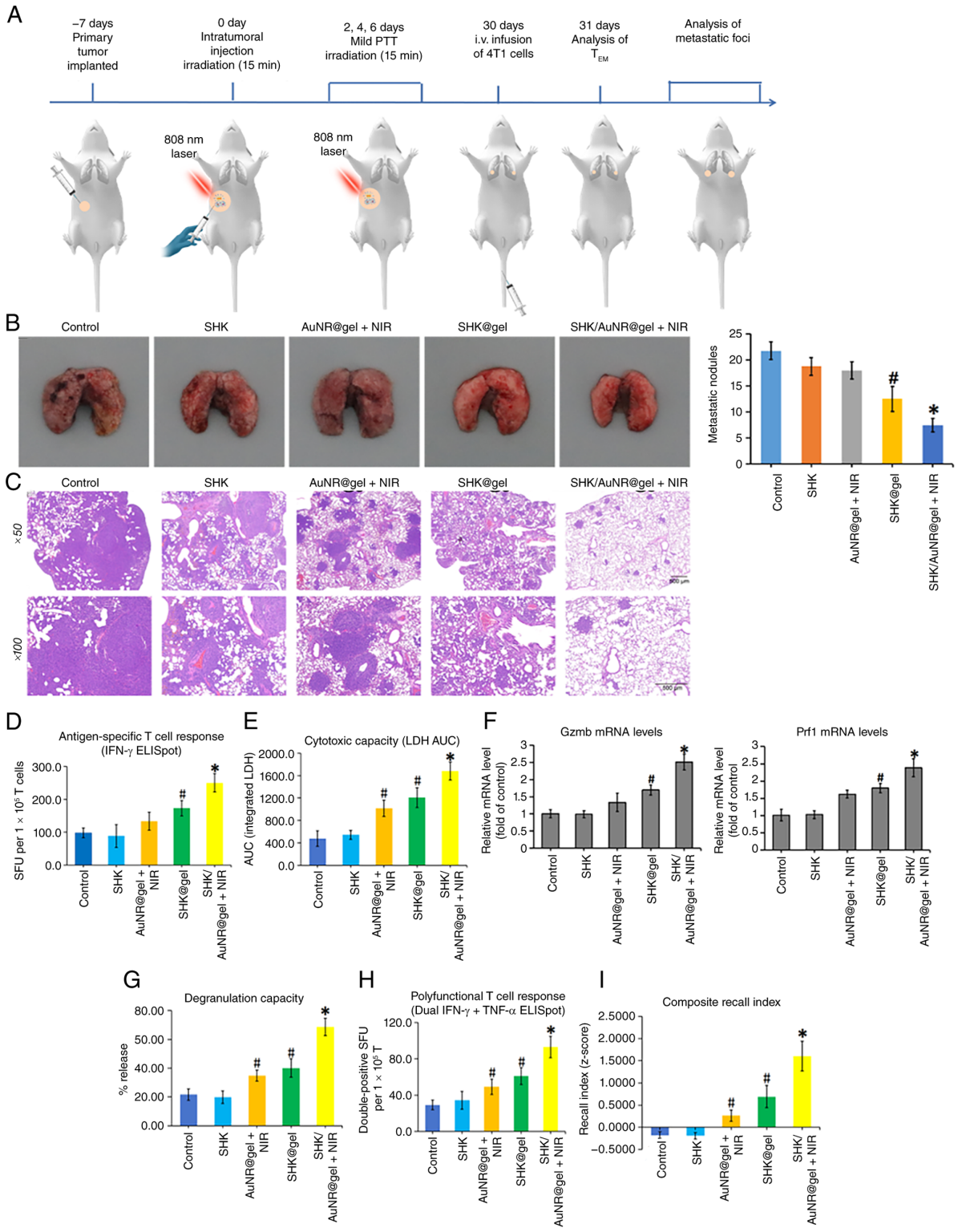

Figure 9. SHK/AuNR@gel + NIR treatment induces a potent and systemic antitumor immune memory. (A) Schematic diagram of the experimental timeline for assessing lung metastasis. (B) Representative images (upper) and quantitative analysis (lower) of metastatic lung nodules in different groups (n=4). (C) Representative H&E-stained sections of lung tissues. Scale bars, 500 μm. (D) Antigen-specific T cell response. The frequency of IFN-γ-producing T cells in response to 4T1 tumor lysates was measured by ELISpot (antigen-presenting cells: magnetically isolated CD11c$^+$ DCs pulsed with 4T1 lysates for 2-4 h and thoroughly washed; APC: T=1:10) and is presented as spot-forming units per 10^5 T cells (n=4). (E) Cytotoxic capacity of memory CD8$^+$ T cells. The tumor-eliminating activity of enriched CD8$^+$ T cells against 4T1 target cells was assessed by an LDH release assay at the indicated effector-to-target (E: T) ratios. The overall cytotoxicity is summarized by the AUC (n=4). (F) Relative mRNA expression of Gzmb and Prf1 in enriched CD8$^+$ T cells (n=4). (G) Degranulation capacity upon antigen-specific stimulation, presented as the percentage of specific granule release [supernatant/(supernatant + cell lysate) x100%] (n=4). (H) Polyfunctional T cell response. The frequency of T cells simultaneously producing IFN-γ and TNF-α upon antigen recall was determined by dual-color ELISpot and is shown as double-positive spots per 10^5 T cells (n=4). (I) Comprehensive recall cytokine signature. A composite recall index was calculated from the levels of multiple cytokines (IFN-γ, TNF-α, IL-2, CXCL9 and CXCL10) in the supernatant of re-stimulated untouched T cells co-cultured with pulsed CD11c$^+$ DCs (n=4). All data are presented as the mean ± SD. $^{\#}$P<0.05 vs. the Control group, *P<0.05 vs. the SHK@gel group. SHK, shikonin; AuNRs, gold nanorods; NIR, near-infrared irradiation; LDH, lactate dehydrogenase; AUC, area under the dose-response curve; Gzmb, granzyme B; Prf1, perforin 1; DCs, dendritic cells.

of key cytolytic effector molecules was analyzed, and degranulation capacity was assessed. qPCR analysis revealed that the enriched $CD8^+$ T cells from the SHK/AuNR@gel + NIR group expressed significantly higher levels of *Gzmb* and *Prf1* (Fig. 9F). Consistent with this finding, antigen-restimulated $CD8^+$ T cells from the same group exhibited a significantly greater degree of degranulation, as reflected by the release of these cytolytic effectors upon antigen-specific stimulation (Fig. 9G). Beyond cytotoxic potency, the protective efficacy of memory T cells is strongly influenced by their functional quality, particularly their capacity for polyfunctional cytokine production. To evaluate this property, a dual-color ELISpot assay was employed to quantify T cells capable of simultaneously producing IFN-γ and TNF-α following antigen recall. The frequency of these polyfunctional T cells, expressed as double-positive SFU per 10^5 T cells, was significantly increased in the SHK/AuNR@gel + NIR group compared with all other treatment groups (Fig. 9H). To obtain a broader overview of the recall immune response, a panel of cytokines and chemokines in the supernatants of antigen-restimulated splenocytes was further quantified. A composite recall-response index was calculated as the mean z-score of IFN-γ, TNF-α, IL-2, CXCL9 and CXCL10 levels. Notably, the SHK/AuNR@gel + NIR group exhibited the highest recall index among all treatment groups (Fig. 9I). Collectively, these findings demonstrate that a single intratumoral administration of SHK/AuNR@gel combined with mild PTT generates a high-quality and durable antitumor immune memory characterized by strong antigen specificity, potent cytotoxic activity, enhanced degranulation, increased T-cell polyfunctionality, and broad cytokine responsiveness.

Discussion

Conventional systemic chemotherapy for tumors often causes off-target toxicity in normal tissues. By contrast, localized drug delivery systems offer several advantages, including reduced systemic exposure and sustained drug release at the tumor site, thereby improving therapeutic efficacy (64). Various localized delivery platforms, such as hydrogels, nanoparticles, liposomes and micelles, have been investigated. Among these, hydrogels have attracted considerable attention because of their unique physicochemical properties. Hydrogels are three-dimensional networks of crosslinked hydrophilic polymer chains. Injectable hydrogels, which can form gels in the target area, are widely used in biomedical applications, including drug and cell delivery and tissue engineering. In particular, intratumoral drug delivery using injectable hydrogels has become an area of great interest. These hydrogels enable sustained and controlled drug release specifically at the tumor site, thereby minimizing adverse effects caused by systemic drug exposure. In addition, localized therapy with injectable hydrogels can help address the poor solubility of numerous chemotherapeutic agents, reduce the required dose, and increase the amount of drug reaching the tumor site (64). In the present study, a methoxy poly(ethylene glycol)-b-poly(ε-caprolactone-co-1,4,8-trioxa[4.6]spiro-9-undecanone) (mPECT) supramolecular hydrogel was used, which showed excellent photothermal conversion performance, stable drug-release characteristics that were not affected by temperature changes, and favorable biosafety (33). This supramolecular hydrogel effectively supported the objectives of the present study.

ICD is a form of regulated cell death in which dying tumor cells release or expose immunostimulatory danger signals and tumor-associated antigens, thereby promoting DC-mediated antigen presentation and subsequent T-cell priming (8). An increasing number of anticancer therapies have been reported to induce ICD and thereby enhance antitumor immunity. However, numerous ICD-inducing treatments, including radiotherapy (65), PTT (18,61), and chemotherapeutic agents such as paclitaxel (66), doxorubicin (67) and oxaliplatin (68), can simultaneously activate compensatory immunosuppressive mechanisms. In particular, these therapies have been shown to increase PD-L1 expression and/or enhance IDO1 activity during the process of ICD induction. Therefore, they often need to be combined with PD-1/PD-L1 antibodies or IDO1 inhibitors to promote and maintain the long-lasting antitumor immune response. By contrast, in the present study, SHK enhanced ICD-associated signals while attenuating PD-L1 expression and IDO1 activation, suggesting a therapeutically favorable profile that may help counteract immunosuppressive feedback during ICD induction. In line with this functional profile, SHK reduced NF-κB transcriptional activity and inhibited the nuclear translocation of NF-κB p65, which may contribute, at least in part, to PD-L1 downregulation, considering the reported involvement of NF-κB signaling in PD-L1 regulation. In addition, the observed inhibition of IDO1 activity is consistent with previous evidence suggesting that SHK inhibits IDO1 catalytic activity through interaction with the ferric-IDO1 enzyme. Further studies are warranted to more precisely define the direct molecular events linking SHK to PD-L1 regulation and IDO1 inhibition in this localized treatment system.

Recent advances have expanded the understanding of SHK in tumor immunology beyond its conventional direct cytotoxic effects on tumor cells, highlighting its potential role in regulated cell death-mediated immune activation. A recent study has shown that SHK can enhance tumor immunogenicity and improve the response to immune checkpoint blockade, as indicated by increased calreticulin membrane exposure and Hsp70 upregulation, as well as synergistic enhancement of DC activation and $CD8^+$ T-cell responses when combined with PD-1 blockade in tumor models (69). In addition, SHK has been reported to induce ferroptosis through GOT1-mediated ferritinophagy, accompanied by the release of ICD-associated signals, including ATP and HMGB1 (70). Nanomedicine-based studies have further demonstrated that Fe(III)-SHK supramolecular nanomedicines can function as ICD stimulants and multifunctional immunoadjuvants for tumor vaccination (71). Moreover, Fe-SHK metal-phenolic networks have been shown to promote the generation of autologous tumor cell lysates through ferroptosis and necroptosis, thereby contributing to personalized *in situ* nanovaccine-based antitumor immunity (72). More recently, nanosized SHK has been reported to synergize with manganese to enhance the cGAS-STING-mediated interferon response and sensitize tumors to immunotherapy (73).

These findings suggest that the immunomodulatory effects of SHK may involve multiple interconnected

processes, including ICD, ferroptosis/necroptosis and cGAS-STING-associated innate immune activation. The present results are consistent with these recent advances, as local low-dose SHK delivery enhanced ICD-associated signals and suppressed mild PTT-induced IDO1/PD-L1 immunosuppressive feedback, thereby promoting systemic antitumor immunity. However, ferroptosis/necroptosis and cGAS-STING signaling were not directly examined in the present study. Therefore, future studies are required to determine whether these regulated cell death pathways and innate immune signaling events contribute to the long-term systemic antitumor immunity induced by SHK/AuNR@gel plus mild PTT.

In recent years, PD-1/PD-L1 monoclonal antibodies have been approved for the clinical treatment of different types of malignant tumors and are the most common immunotherapeutic strategy at present. Previous research has shown that PD-1/PD-L1 antibody can even cure some patients with advanced tumor metastasis, and its favorable efficacy is encouraging (74). However, PD-1/PD-L1 antibody therapy has several disadvantages. Firstly, most solid tumors have an immunosuppressive microenvironment, lacking a sufficient number of infiltrating immune cells and belonging to the immune 'cold tumor', which leads to a low clinical response rate of PD-1/PD-L1 antibody therapy (75). Secondly, the systemic administration of PD-1/PD-L1 antibody is prone to producing a series of systemic side effects, which trigger the body's autoimmune response and induce the immune system to attack normal tissues. Thirdly, PD-1/PD-L1 antibody therapy is costly, which may increase the global burden of healthcare expenditures. Compared with the PD-1/PD-L1 antibody, the present study has the following potential advantages. Firstly, combining the noninvasive mild PTT with locally administered SHK can trigger immune activation and induce ICD, while suppressing PD-L1 expression and IDO1 activation, thereby contributing to strong and long-lasting antitumor-specific immunity in immune-cold tumors. Secondly, using a hydrogel as the medium, SHK, which is administered only once, can target the local part of the tumor for low-dose sustained release. This may avoid repeated high concentrations of SHK, which is similar to intravenous administration, entering the blood circulation and causing toxic damage to systemic organs. Thirdly, compared with PD-1/PD-L1 antibody therapy, the cost of SHK-based treatment is considered to be markedly lower.

Despite the potential of SHK/AuNR@gel plus mild PTT to induce systemic antitumor immunity, an abscopal effect and immune memory in the present study, several key barriers remain before further clinical translation can be considered. First, although the mPECT hydrogel enabled local retention and sustained release of SHK in the present system, clinically compatible or medical-grade formulations will need to be further established. Future studies should systematically evaluate scalable manufacturing, batch-to-batch consistency, sterilization procedures, degradation products, quality control and regulatory approval pathways (76). Second, AuNRs functioned as the photothermal conversion component for local mild PTT in this system; however, their long-term *in vivo* fate remains an important biosafety concern, including clearance, reticuloendothelial system uptake, accumulation in the liver, spleen and other organs, potential chronic toxicity and dose-related safety (77). Third, intratumoral injection may not be suitable for all patients with TNBC. Its clinical feasibility may be limited by tumor location, lesion size, lesion depth, accessibility, multifocality and the availability of image-guided injection, suggesting that this strategy may be more applicable to accessible or image-guided injectable local lesions (78). Fourth, although an abscopal antitumor effect and long-term immune memory were observed in the mouse models used in the present study, these preclinical findings are not sufficient to suggest that this local treatment strategy could directly replace current standard systemic therapies. A more appropriate translational positioning may be to develop this approach as a local *in situ* immune-priming or immune-sensitizing strategy that could be rationally integrated with current neoadjuvant chemotherapy or immune checkpoint blockade in selected patients suitable for intratumoral intervention (79). Further formulation optimization, long-term safety evaluation and clinically relevant studies combining this strategy with standard treatments are still required to support its further translational development.

In conclusion, the present study demonstrates that mPECT hydrogel-mediated local administration of SHK/AuNR@gel combined with mild PTT can remodel the immunosuppressive TME, enhance ICD-associated immune activation, and suppress IDO1/PD-L1-mediated immunosuppressive feedback in immune-cold TNBC models. This localized combination strategy inhibited primary tumor growth, induced an abscopal antitumor effect against untreated distant tumors, and generated durable antitumor immune memory. In addition, the mPECT hydrogel enabled prolonged local retention and sustained release of SHK, thereby reducing rapid systemic exposure. Taken together, these findings provide a preclinical basis for the further development of localized SHK-based combination strategies, particularly for therapeutic agents with antitumor potential but limited by systemic toxicity.

Acknowledgements

Not applicable.

Funding

The present study was supported by grants from the National Natural Science Foundation of China (grant no. 82100008), the Natural Science Foundation of Shaanxi (grant no. 2019JQ889), the State Key Laboratory of Cancer Biology of China (grant no. CBSKL201710) and the Foundation of Xi'an Medical University (grant no. 2018DOC02).

Availability of data and materials

The data generated in the present study may be requested from the corresponding author.

Authors' contributions

TP and FZ conceived and designed the study. ZF and TP synthesized and characterized the hydrogel. TP and TS performed the experiments. Jun Jiang assisted with the experiments. FZ

analyzed the data and prepared the figures. TP and TS drafted the manuscript. FZ revised the manuscript. All authors read and approved the final version of the manuscript. All authors agree to be accountable for all aspects of the work and to ensure that questions related to the accuracy or integrity of any part of the work are appropriately investigated and resolved. TP and FZ confirm the authenticity of all the raw data.

Ethics approval and consent to participate

All animal experiments were approved by the Animal Ethics Committee of Air Force Medical University (approval no. 20241327; Xi'an, China) and were covered by the Laboratory Animal Use License SYXK (Shaan) 2024-003. All procedures were performed in accordance with institutional guidelines and the ARRIVE guidelines.

Patient consent for publication

Not applicable.

Competing interests

The authors declare that they have no competing interests.

References

1. Guo C, He J, Song X, Tan L, Wang M, Jiang P, Li Y, Cao Z and Peng C: Pharmacological properties and derivatives of shikonin-A review in recent years. Pharmacol Res 149: 104463, 2019.
2. Abdulridha MK, Al-Marzoqi AH, Al-Awsi GRL, Mubarak SMH, Heidarifard M and Ghasemian A: Anticancer effects of herbal medicine compounds and novel formulations: A literature review. J Gastrointest Cancer 51: 765-773, 2020.
3. Boulos JC, Rahama M, Hegazy MF and Efferth T: Shikonin derivatives for cancer prevention and therapy. Cancer Lett 459: 248-267, 2019.
4. Wang R, Yin R, Zhou W, Xu D and Li S: Shikonin and its derivatives: A patent review. Expert Opin Ther Pat 22: 977-997, 2012.
5. Cheng Z, Li M, Dey R and Chen Y: Nanomaterials for cancer therapy: Current progress and perspectives. J Hematol Oncol 14: 85, 2021.
6. Li S, Zhang T, Xu W, Ding J, Yin F, Xu J, Sun W, Wang H, Sun M, Cai Z and Hua Y: Sarcoma-targeting peptide-decorated polypeptide nanogel intracellularly delivers shikonin for upregulated osteosarcoma necroptosis and diminished pulmonary metastasis. Theranostics 8: 1361-1375, 2018.
7. Korangath P, Barnett JD, Sharma A, Henderson ET, Stewart J, Yu SH, Kandala SK, Yang CT, Caserto JS, Hedayati M, *et al*: Nanoparticle interactions with immune cells dominate tumor retention and induce T cell-mediated tumor suppression in models of breast cancer. Sci Adv 6: eaay1601, 2020.
8. Ahmed A and Tait SWG: Targeting immunogenic cell death in cancer. Mol Oncol 14: 2994-3006, 2020.
9. Wang H, Tang Y, Fang Y, Zhang M, Wang H, He Z, Wang B, Xu Q and Huang Y: Reprogramming tumor immune microenvironment (TIME) and metabolism via biomimetic targeting codelivery of shikonin/JQ1. Nano Lett 19: 2935-2944, 2019.
10. Li J, Zhao M, Sun M, Wu S, Zhang H, Dai Y and Wang D: Multifunctional nanoparticles boost cancer immunotherapy based on modulating the immunosuppressive tumor microenvironment. ACS Appl Mater Interfaces 12: 50734-50747, 2020.
11. Guo W, Yao S, Sun P, Yang TB, Tang CP, Zheng MY, Ye Y and Meng LH: Discovery and characterization of natural products as novel indoleamine 2,3-dioxygenase 1 inhibitors through high-throughput screening. Acta Pharmacol Sin 41: 423-431, 2020.
12. Nasrollahzadeh Sabet M, Biglari S, Khorram Khorshid HR and Esmaeilzadeh E: Shikonin ameliorates experimental autoimmune encephalomyelitis (EAE) via immunomodulatory, anti-apoptotic and antioxidative activity. J Pharm Pharmacol 72: 1970-1976, 2020.
13. Zhou F, Wu S, Song S, Chen WR, Resasco DE and Xing D: Antitumor immunologically modified carbon nanotubes for photothermal therapy. Biomaterials 33: 3235-3242, 2012.
14. Orosz P, Echtenacher B, Falk W, Rüschoff J, Weber D and Männel DN: Enhancement of experimental metastasis by tumor necrosis factor. J Exp Med 177: 1391-1398, 1993.
15. Frey B, Weiss EM, Rubner Y, Wunderlich R, Ott OJ, Sauer R, Fietkau R and Gaipl US: Old and new facts about hyperthermia-induced modulations of the immune system. Int J Hyperthermia 28: 528-542, 2012.
16. Li Y, He L, Dong H, Liu Y, Wang K, Li A, Ren T, Shi D and Li Y: Fever-inspired immunotherapy based on photothermal CpG nanotherapeutics: The critical role of mild heat in regulating tumor microenvironment. Adv Sci (Weinh) 5: 1700805, 2018.
17. Payne M, Bossmann SH and Basel MT: Direct treatment versus indirect: Thermo-ablative and mild hyperthermia effects. Wiley Interdiscip Rev Nanomed Nanobiotechnol 12: e1638, 2020.
18. Peng J, Xiao Y, Li W, Yang Q, Tan L, Jia Y, Qu Y and Qian Z: Combined photothermal therapy and immunotherapy: Photosensitizer micelles together with IDO inhibitor enhance cancer photothermal therapy and immunotherapy (Adv. Sci. 5/2018). Adv Sci (Weinh) 5: 1870031, 2018.
19. Liu X, Su Q, Song H, Shi X, Zhang Y, Zhang C, Huang P, Dong A, Kong D and Wang W: PolyTLR7/8a-conjugated, antigen-trapping gold nanorods elicit anticancer immunity against abscopal tumors by photothermal therapy-induced in situ vaccination. Biomaterials 275: 120921, 2021.
20. Bai X, Ni J, Beretov J, Graham P and Li Y: Immunotherapy for triple-negative breast cancer: A molecular insight into the microenvironment, treatment, and resistance. J Natl Cancer Cent 1: 75-87, 2021.
21. Kim H, Choi JM and Lee KM: Immune checkpoint blockades in triple-negative breast cancer: Current state and molecular mechanisms of resistance. Biomedicines 10: 1130, 2022.
22. Li ZL, Zhang HL, Huang Y, Huang JH, Sun P, Zhou NN, Chen YH, Mai J, Wang Y, Yu Y, *et al*: Autophagy deficiency promotes triple-negative breast cancer resistance to T cell-mediated cytotoxicity by blocking tenascin-C degradation. Nat Commun 11: 3806, 2020.
23. Song X, Zhou Z, Li H, Xue Y, Lu X, Bahar I, Kepp O, Hung MC, Kroemer G and Wan Y: Pharmacologic Suppression of B7-H4 glycosylation restores antitumor immunity in immune-cold breast cancers. Cancer Discov 10: 1872-1893, 2020.
24. Keenan TE and Tolaney SM: Role of immunotherapy in triple-negative breast cancer. J Natl Compr Canc Netw 18: 479-489, 2020.
25. Revuri V, Rajendrakumar SK, Park MS, Mohapatra A, Uthaman S, Mondal J, Bae WK, Park IK and Lee YK: Heat-confined tumor-docking reversible thermogel potentiates systemic antitumor immune response during near-infrared photothermal ablation in triple-negative breast cancer. Adv Healthc Mater 10: e2100907, 2021.
26. Wu C, Xu J, Xie Z, Huang H, Li N, Wei X, Li T, Yang H, Li S, Qin X and Liu Y: Light-responsive hyaluronic acid nanomicelles co-loaded with an IDO inhibitor focus targeted photoimmunotherapy against 'immune cold' cancer. Biomater Sci 9: 8019-8031, 2021.
27. Wang W, Wu Y, Chen S, Liu X, He J, Wang S, Lu W, Tang Y and Huang J: Shikonin is a novel and selective IMPDH2 inhibitor that target triple-negative breast cancer. Phytother Res 35: 463-476, 2021.
28. National Research Council (US) Committee for the Update of the Guide for the Care and Use of Laboratory Animals: Guide for the care and use of laboratory animals. 8th edition. Washington (DC): National Academies Press (US), 2011.
29. European Parliament and Council of the European Union: Directive 2010/63/EU of the European Parliament and of the Council of 22 September 2010 on the protection of animals used for scientific purposes. In: Official Journal of the European Union Publications Office of the European Union, Luxembourg, pp33-79, 2010.
30. Workman P, Aboagye EO, Balkwill F, Balmain A, Bruder G, Chaplin DJ, Double JA, Everitt J, Farningham DA, Glennie MJ, *et al*: Guidelines for the welfare and use of animals in cancer research. Br J Cancer 102: 1555-1577, 2010.
31. Xiang Y, Xiao M, Han S, Xu S, Cao Y, Lv Z, Liu J, Liu J, Deng L and Dong A: Preparation and investigation of high solid content PTX-loaded nanoparticles dispersion via nanoprecipitation method. J Biomater Sci Polym Ed 25: 1144-1158, 2014.

32. Yin L, Xu S, Feng Z, Deng H, Zhang J, Gao H, Deng L, Tang H and Dong A: Supramolecular hydrogel based on high-solid-content mPECT nanoparticles and cyclodextrins for local and sustained drug delivery. Biomater Sci 5: 698-706, 2017.
33. Liu M, Huang P, Wang W, Feng Z, Zhang J, Deng L and Dong A: An injectable nanocomposite hydrogel co-constructed with gold nanorods and paclitaxel-loaded nanoparticles for local chemo-photothermal synergetic cancer therapy. J Mater Chem B 7: 2667-2677, 2019.
34. Ali MRK, Snyder B and El-Sayed MA: Synthesis and optical properties of small Au nanorods using a seedless growth technique. Langmuir 28: 9807-9815, 2012.
35. Xu S, Yin L, Xiang Y, Deng H, Deng L, Fan H, Tang H, Zhang J and Dong A: Supramolecular hydrogel from nanoparticles and cyclodextrins for local and sustained nanoparticle delivery. Macromol Biosci 16: 1188-1199, 2016.
36. Pan T, Zhang F, Li F, Gao X, Li Z, Li X and Ren X: Shikonin blocks human lung adenocarcinoma cell migration and invasion in the inflammatory microenvironment via the IL-6/STAT3 signaling pathway. Oncol Rep 44: 1049-1063, 2020.
37. Pan T, Chang Y, He M, He Z, Jiang J, Ren X and Zhang F: β-Hydroxyisovalerylshikonin regulates macrophage polarization via the AMPK/Nrf2 pathway and ameliorates sepsis in mice. Pharm Biol 60: 729-742, 2022.
38. Zhang F, Pan T, Wu X, Gao X, Li Z and Ren X: Non-cytotoxic doses of shikonin inhibit lipopolysaccharide-induced TNF-α expression via activation of the AMP-activated protein kinase signaling pathway. Exp Ther Med 20: 45, 2020.
39. Feng B, Hou B, Xu Z, Saeed M, Yu H and Li Y: Self-amplified drug delivery with light-inducible nanocargoes to enhance cancer immunotherapy. Adv Mater 31: e1902960, 2019.
40. Tu J, Xu H, Ma L, Li C, Qin W, Chen X, Yi M, Sun L, Liu B and Yuan X: Nintedanib enhances the efficacy of PD-L1 blockade by upregulating MHC-I and PD-L1 expression in tumor cells. Theranostics 12: 747-766, 2022.
41. Si Y, Yue J, Liu Z, Li M, Du F, Wang X, Dai Z, Hu N, Ju J, Gao S, *et al*: Phase-transformation nanoparticle-mediated sonodynamic therapy: An effective modality to enhance anti-tumor immune response by inducing immunogenic cell death in breast cancer. Int J Nanomedicine 16: 1913-1926, 2021.
42. Livak KJ and Schmittgen TD: Analysis of relative gene expression data using real-time quantitative PCR and the 2(-Delta Delta C(T)) method. Methods 25: 402-408, 2001.
43. Banchereau J and Steinman RM: Dendritic cells and the control of immunity. Nature 392: 245-252, 1998.
44. Trinchieri G: Interleukin-12 and the regulation of innate resistance and adaptive immunity. Nat Rev Immunol 3: 133-146, 2003.
45. Danaher P, Warren S, Dennis L, D'Amico L, White A, Disis ML, Geller MA, Odunsi K, Beechem J and Fling SP: Gene expression markers of tumor infiltrating leukocytes. J Immunother Cancer 5: 18, 2017.
46. Rooney MS, Shukla SA, Wu CJ, Getz G and Hacohen N: Molecular and genetic properties of tumors associated with local immune cytolytic activity. Cell 160: 48-61, 2015.
47. Sakaguchi S, Yamaguchi T, Nomura T and Ono M: Regulatory T cells and immune tolerance. Cell 133: 775-787, 2008.
48. Qiu N, Liu Y, Liu Q, Chen Y, Shen L, Hu M, Zhou X, Shen Y, Gao J and Huang L: Celastrol nanoemulsion induces immunogenicity and downregulates PD-L1 to boost abscopal effect in melanoma therapy. Biomaterials 269: 120604, 2021.
49. Oba T, Long MD, Keler T, Marsh HC, Minderman H, Abrams SI, Liu S and Ito F: Overcoming primary and acquired resistance to anti-PD-L1 therapy by induction and activation of tumor-residing cDC1s. Nat Commun 11: 5415, 2020.
50. Brackett CM, Kojouharov B, Veith J, Greene KF, Burdelya LG, Gollnick SO, Abrams SI and Gudkov AV: Toll-like receptor-5 agonist, entolimod, suppresses metastasis and induces immunity by stimulating an NK-dendritic-CD8+ T-cell axis. Proc Natl Acad Sci USA 113: E874-E883, 2016.
51. Hartung T: Comparative analysis of the revised directive 2010/63/EU for the protection of laboratory animals with its predecessor 86/609/EEC-a t4 report. ALTEX 27: 285-303, 2010.
52. Jin L, Shen S, Huang Y, Li D and Yang X: Corn-like Au/Ag nanorod-mediated NIR-II photothermal/photodynamic therapy potentiates immune checkpoint antibody efficacy by reprogramming the cold tumor microenvironment. Biomaterials 268: 120582, 2021.
53. Draganov D, Han Z, Rana A, Bennett N, Irvine DJ and Lee PP: Ivermectin converts cold tumors hot and synergizes with immune checkpoint blockade for treatment of breast cancer. NPJ Breast Cancer 7: 22, 2021.
54. Gajewski TF, Meng Y, Blank C, Brown I, Kacha A, Kline J and Harlin H: Immune resistance orchestrated by the tumor microenvironment. Immunol Rev 213: 131-145, 2006.
55. Jiang X, Wang J, Deng X, Xiong F, Ge J, Xiang B, Wu X, Ma J, Zhou M, Li X, *et al*: Role of the tumor microenvironment in PD-L1/PD-1-mediated tumor immune escape. Mol Cancer 18: 10, 2019.
56. Yu Z, Gao J, Zhang X, Peng Y, Wei W, Xu J, Li Z, Wang C, Zhou M, Tian X, *et al*: Characterization of a small-molecule inhibitor targeting NEMO/IKKβ to suppress colorectal cancer growth. Signal Transduct Target Ther 7: 71, 2022.
57. Sun Q, Gong T, Liu M, Ren S, Yang H, Zeng S, Zhao H, Chen L, Ming T, Meng X and Xu H: Shikonin, a naphthalene ingredient: Therapeutic actions, pharmacokinetics, toxicology, clinical trials and pharmaceutical researches. Phytomedicine 94: 153805, 2022.
58. Antonangeli F, Natalini A, Garassino MC, Sica A, Santoni A and Di Rosa F: Regulation of PD-L1 expression by NF-κB in cancer. Front Immunol 11: 584626, 2020.
59. Chen HM, Wang PH, Chen SS, Wen CC, Chen YH, Yang WC and Yang NS: Shikonin induces immunogenic cell death in tumor cells and enhances dendritic cell-based cancer vaccine. Cancer Immunol Immunother 61: 1989-2002, 2012.
60. Huang Z, Chen Y, Zhang J, Li W, Shi M, Qiao M, Zhao X, Hu H and Chen D: Laser/GSH-activatable oxaliplatin/phthalocyanine-based coordination polymer nanoparticles combining chemophotodynamic therapy to improve cancer immunotherapy. ACS Appl Mater Interfaces 13: 39934-39948, 2021.
61. Huang L, Li Y, Du Y, Zhang Y, Wang X, Ding Y, Yang X, Meng F, Tu J, Luo L and Sun C: Mild photothermal therapy potentiates anti-PD-L1 treatment for immunologically cold tumors via an all-in-one and all-in-control strategy. Nat Commun 10: 4871, 2019.
62. Zheng Y and Rudensky AY: Foxp3 in control of the regulatory T cell lineage. Nat Immunol 8: 457-462, 2007.
63. Thakur R, Trivedi R, Rastogi N, Singh M and Mishra DP: Inhibition of STAT3, FAK and Src mediated signaling reduces cancer stem cell load, tumorigenic potential and metastasis in breast cancer. Sci Rep 5: 10194, 2015.
64. Norouzi M, Nazari B and Miller DW: Injectable hydrogel-based drug delivery systems for local cancer therapy. Drug Discov Today 21: 1835-1849, 2016.
65. Sato H, Okonogi N and Nakano T: Rationale of combination of anti-PD-1/PD-L1 antibody therapy and radiotherapy for cancer treatment. Int J Clin Oncol 25: 801-809, 2020.
66. Yang Q, Shi G, Chen X, Lin Y, Cheng L, Jiang Q, Yan X, Jiang M, Li Y, Zhang H, *et al*: Nanomicelle protects the immune activation effects of Paclitaxel and sensitizes tumors to anti-PD-1 Immunotherapy. Theranostics 10: 8382-8399, 2020.
67. Liu Y, Xie J, Zhao X, Zhang Y, Zhong Z and Deng C: A polymeric IDO inhibitor based on poly(ethylene glycol)-b-poly(L-tyrosine-co-1-methyl-D-tryptophan) enables facile trident cancer immunotherapy. Biomater Sci 10: 5731-5743, 2022.
68. Feng B, Zhou F, Hou B, Wang D, Wang T, Fu Y, Ma Y, Yu H and Li Y: Binary cooperative prodrug nanoparticles improve immunotherapy by synergistically modulating immune tumor microenvironment. Adv Mater 30: 1803001, 2018.
69. Chen J, Liu J, Liu X, Wang J, Wang X, Ye X, Xie Q, Liang J and Li Y: Shikonin improves the effectiveness of PD-1 blockade in colorectal cancer by enhancing immunogenicity via Hsp70 upregulation. Mol Biol Rep 51: 86, 2024.
70. Li W, Fu H, Fang L, Chai H, Gao T, Chen Z and Qian S: Shikonin induces ferroptosis in multiple myeloma via GOT1-mediated ferritinophagy. Front Oncol 12: 1025067, 2022.
71. Feng W, Shi W, Cui Y, Xu J, Liu S, Gao H, Zhu S, Liu Y and Zhang H: Fe(III)-Shikonin supramolecular nanomedicines as immunogenic cell death stimulants and multifunctional immunoadjuvants for tumor vaccination. Theranostics 13: 5266-5289, 2023.
72. Shi W, Feng W, Li S, Cui Y, Liu S, Jiang H, Liu Y and Zhang H: Ferroptosis and necroptosis produced autologous tumor cell lysates co-delivering with combined Immnoadjuvants as personalized in situ nanovaccines for antitumor immunity. ACS Nano 17: 14475-14493, 2023.
73. Yu S, Li J, Zhang J, Zeng G, Zeng B, Song S, Lao Z, Chen H, Wen Z, Yang Z, *et al*: Nanosized shikonin disrupts tumor-cell mismatch repair and synergizes with manganese to sensitize squamous carcinoma to immunotherapy. ACS Nano 19: 13889-13905, 2025.

74. Pardoll DM: The blockade of immune checkpoints in cancer immunotherapy. Nat Rev Cancer 12: 252-264, 2012.
75. Majidpoor J and Mortezaee K: The efficacy of PD-1/PD-L1 blockade in cold cancers and future perspectives. Clin Immunol 226: 108707, 2021.
76. Carballo-Pedrares N, Giménez VMM and Alonso MJ: Clinical translation of injectable hydrogels: From bioactive polymers to long-acting drug delivery systems. Drug Deliv Transl Res 16: 1685-1708, 2026.
77. Lankveld DP, Rayavarapu RG, Krystek P, Oomen AG, Verharen HW, van Leeuwen TG, de Jong WH and Manohar S: Blood clearance and tissue distribution of PEGylated and non-PEGylated gold nanorods after intravenous administration in rats. Nanomedicine (Lond) 6: 339-349, 2011.
78. Sheth RA, Wehrenberg-Klee E, Patel SP, Brock KK, Fotiadis N and de Baère T: Intratumoral injection of immunotherapeutics: State of the art and future directions. Radiology 312: e232654, 2024.
79. Schmid P, Cortes J, Dent R, McArthur H, Pusztai L, Kümmel S, Denkert C, Park YH, Hui R, Harbeck N, *et al*: Overall survival with pembrolizumab in early-stage triple-negative breast cancer. N Engl J Med 391: 1981-1991, 2024.